

AD-A273 837



①

AFIT/GSO/ENP/93D-03

S DTIC
ELECTE
DEC 16 1993
A

OBJECTIVE IMAGE QUALITY METRICS:
APPLICATIONS FOR PARTIALLY COMPENSATED
IMAGES OF SPACE OBJECTS

THESIS
David J. Lee
Captain, USAF

AFIT/GSO/ENP/93D-03

93-30515



Approved for public release; distribution unlimited

98 12 151 29

OBJECTIVE IMAGE QUALITY METRICS:
APPLICATIONS FOR PARTIALLY COMPENSATED
IMAGES OF SPACE OBJECTS

THESIS

Presented to the Faculty of the Graduate School of Engineering
of the Air Force Institute of Technology
Air University
In Partial Fulfillment of the
Requirements for the Degree of
Master of Science in Space Operations

David J. Lee, B.Sci., Electrical and Electronics Engineering
Captain, USAF

December 15, 1993

Approved for public release; distribution unlimited

Accession For		1
NTIS	CRA&I	<input checked="" type="checkbox"/>
DTIC	TAB	<input type="checkbox"/>
Unannounced		<input type="checkbox"/>
Justification		
By		
Distribution /		
Availability Codes		
Dist	Avail and/or Special	
A-1		



Preface

The most important lesson a student can learn during a thesis effort (besides time management) is teamwork. The most important example of this in my thesis research is the teamwork between my wife and myself. My contribution to the team effort consisted of schoolwork. Denise's contribution to the team effort consisted of everything else: balancing the checkbook, paying bills, taking the car to the garage, mowing the lawn, cleaning the house, and all the other things I didn't have time to do. She already knows how much I appreciate her sacrifices over the last months, and now you, the reader, know as well.

The other important example of teamwork in this effort is between myself and my advisor, Dr. Mike Roggemann. I felt fortunate that I was independent enough to make this thesis my own, yet felt I had ample guidance when running up against the inevitable brick wall. Also, hopefully Dr. Roggemann knows how much my classmates and I appreciate him opening "Father Roggemann's Home for Wayward Space Operations Students" by advising so many out-of-department theses.

Thanks also to Drs. Welsh and Chan for their help in my research effort.

David J. Lee

Table of Contents

	Page
Preface	ii
List of Figures	v
Abstract	viii
I. Introduction	1-1
1.1 Background	1-1
1.1.1 Imaging of Orbiting Satellites	1-1
1.1.2 Hybrid Imaging	1-3
1.2 The Image Quality Problem	1-12
1.3 Research Objective	1-12
1.4 Scope	1-13
1.5 Summary of Key Results	1-13
1.6 Document Organization	1-14
II. Image Quality Metrics	2-1
2.1 The Fourier Transform and Image Quality	2-1
2.1.1 Human Visual System Transfer Function	2-2
2.1.2 Spectral Image Quality Metric	2-4
2.2 Histograms and Image Quality	2-7
2.2.1 Histogram-Based Image Quality Metrics	2-7
2.2.2 Histogram Features as Structure Factors	2-10
2.2.3 Histogram Features as Sharpness Functions	2-10
2.2.4 Histogram Features, Information Theory, and Entropy	2-12

	Page
2.2.5 Histogram-Based Image Quality Metrics with Spatial Filtering	2-14
2.3 Summary	2-17
III. Research Approach	3-1
3.1 Adaptive Optics Simulation Software	3-1
3.2 Testing Parameters	3-4
IV. Results	4-1
4.1 Introduction	4-1
4.2 Spectral Image Quality Metrics	4-2
4.3 Histogram-Based Image Quality Metrics	4-7
4.4 Reconstructed Image Selection	4-15
4.5 Summary of Results	4-26
V. Conclusions and Recommendations	5-1
5.1 Thesis Summary	5-1
5.2 Further Research	5-3
5.3 Conclusion	5-4
Appendix A. IQM Results for RORSAT and EORSAT Raw Imagery	A-1
Bibliography	BIB-1
Vita	VITA-1

List of Figures

Figure	Page
1.1. Adaptive Optics Concept	1-3
1.2. AMOS Compensated Imaging System	1-4
1.3. Linear System Model	1-5
1.4. Linear System Model With Detection Noise	1-7
1.5. Ensemble-Averaged Satellite Image	1-8
1.6. Modulus of FFT of Satellite Image	1-8
1.7. Ensemble-Averaged Star Image (Point Spread Function Estimate)	1-9
1.8. Magnitude of the Ensemble-Averaged OTF	1-9
1.9. Inverse Filtering Noise Filter	1-10
1.10. Reconstructed Image Spectrum	1-11
1.11. Reconstructed Satellite Image	1-11
2.1. Frequency Response of HVS	2-3
2.2. Okean Satellite, $r_o = 5$ (left) and 15 (right) cm respectively . . .	2-4
2.3. Spectral Comparison of Different Quality Images	2-5
2.4. Histograms of Good and Bad Images, (normalized to the same energy)	2-8
2.5. Spatial Filter General Mask	2-15
2.6. Sobel Operator Masks	2-16
2.7. Sobel Operator Examples - Left: Original Images - Right: Sobel Filtered Images	2-17
3.1. Block Diagram Description of Adaptive Optics Simulation Software	3-2
3.2. Okean Satellite CAD Drawing	3-3
3.3. Okean Satellite, 4th magnitude, $r_o = 13, 10,$ and 7 cm respectively	3-3

Figure	Page
3.4. Okean Satellite, $r_o = 13cm$, 4th, 5th, and 6th magnitudes respectively	3-3
3.5. Eorsat and Rorsat Imaging Target CAD Drawings	3-4
4.1. Radially Averaged Magnitude Spectra, $r_o = 10$ cm, 5 Different Magnitudes, Okean Satellite Image	4-3
4.2. Radially Averaged Magnitude Spectra, 4th Magnitude, 3 Different r_o 's, Okean Satellite Image	4-4
4.3. Spectral IQM Parameterization, Okean Satellite Image	4-5
4.4. Spectral IQM vs Fried Parameter, Okean Satellite Image	4-6
4.5. Spectral IQM vs Target Magnitude, Okean Satellite Image	4-6
4.6. Spectral IQM vs RMS Error, Okean Satellite Image	4-7
4.7. Variance IQM Parameterization, Okean Satellite Image	4-8
4.8. Variance IQM vs Fried Parameter, Okean Satellite Image	4-8
4.9. Variance IQM vs. Target Magnitude, Okean Satellite Image	4-9
4.10. Okean Satellite, $r_o = 7cm$ and magnitudes of 6,7, and 8 Respectively	4-9
4.11. Sobel-Variance IQM Parameterization, Okean Satellite Image	4-10
4.12. Sobel-Variance IQM vs Fried Parameter, Okean Satellite Image	4-11
4.13. Sobel-Variance IQM vs Target Magnitude, Okean Satellite Image	4-11
4.14. Variance IQM vs. RMS error, Okean Satellite Image	4-12
4.15. Sobel-Variance IQM vs. RMS error, Okean Satellite Image	4-13
4.16. Entropy vs. r_o (cm), Okean Satellite Image	4-14
4.17. Entropy vs. Magnitude, Okean Satellite Image	4-15
4.18. Okean Target Reconstructed Images, High SNR, $r_o = 5cm$, Noise Filter Base Radii = 4,8,12,16,20,24,28, and 32 Pixels Respectively, From Left to Right, Top to Bottom	4-17
4.19. IQM Selection of Noise Filter Radius, Okean Target Reconstructed Images, High SNR, $r_o = 5cm$	4-18

Figure	Page
4.20. Okean Target Reconstructed Images, 6th magnitude, $r_o = 10\text{cm}$, Noise Filter Base Radii = 4,8,12,16,20,24,28, and 32 Pixels Respectively, From Left to Right, Top to Bottom	4-19
4.21. IQM Selection of Noise Filter Radi, Okean Target Reconstructed Images, 6th magnitude, $r_o = 10\text{cm}$	4-20
4.22. Eorsat Target Reconstructed Images, 5th magnitude, $r_o = 7\text{cm}$, Noise Filter Base Radii = 4,8,12,16,20,24,28, and 32 Pixels Respectively, From Left to Right, Top to Bottom	4-22
4.23. IQM Selection of Noise Filter Radius, Eorsat Target Reconstructed Images, 5th magnitude, $r_o = 7\text{cm}$	4-23
4.24. Spectral IQM vs. r_o and Noise Filter Radius, Okean Satellite Image, Magnitude = 4	4-24
4.25. Spectral IQM vs. Target Magnitude and Noise Filter Radius, Okean Satellite Image, $r_o = 10\text{ cm}$	4-24
4.26. Sobel-Variance IQM vs. r_o and Noise Filter Radius, Okean Satellite Image, Magnitude = 4	4-25
4.27. Sobel-Variance IQM vs. Target Magnitude and Noise Filter Radius, Okean Satellite Image, $r_o = 10\text{ cm}$	4-25
A.1. Spectral IQM vs Tried Parameter, RORSAT Image	A-1
A.2. Spectral IQM vs Target Magnitude, RORSAT Image	A-2
A.3. Spectral IQM vs Fried Parameter, EORSAT Satellite Image	A-2
A.4. Spectral IQM vs Target Magnitude, EORSAT Image	A-3
A.5. Sobel-Variance IQM vs Fried Parameter, RORSAT Image	A-3
A.6. Sobel-Variance IQM vs Target Magnitude, RORSAT Image	A-4
A.7. Sobel-Variance IQM vs Fried Parameter, EORSAT Image	A-4
A.8. Sobel-Variance IQM vs Target Magnitude, EORSAT Image	A-5

Abstract

Digital image reconstruction tasks currently require human intervention for a subjective evaluation of image quality. A method for un-supervised measurement of digital image quality is desired. This research investigated various parameters (metrics) that can be automatically extracted from a digital image and tested how well they correlated with image quality. Specifically, images of orbiting satellites captured by a partially compensated adaptive optics telescope were dealt with.

Two different types of quantities were investigated: 1) Fourier spectral parameters, based on the spatial-frequency sensitivities of the HVS; and 2) Histogram shape parameters (i.e image statistical moments) giving quantitative insight into the structural content, information content, and brightness distribution of an image.

An atmospheric imaging simulator was used to generate a test database of images. The use of simulated imagery allowed precise control of the imaging parameters directly relating to image quality: 1) Root Mean Square Error; 2) Seeing conditions (Fried Parameter, r_0); and 3) Target magnitude. This in turn allowed quantitative testing of candidate image quality metrics. Metrics could also be tested against the user defined parameters of the reconstruction process, as a proof-of-concept for totally un-supervised image reconstruction. Finally, based on this testing, two successful image quality metrics are recommended.

Applications that require automatic evaluation of relative image quality should prove feasible. Applications of interest to the thesis sponsor include: 1) "sifting" large numbers of image frames to exclude "bad" images from further processing; and 2) selecting the best reconstructed image to forward to customers.

OBJECTIVE IMAGE QUALITY METRICS: APPLICATIONS FOR PARTIALLY COMPENSATED IMAGES OF SPACE OBJECTS

I. Introduction

1.1 Background

This research is concerned with the measurement of the "quality" of a digital image, specifically the digital images captured and processed at the Air Force Maui Optical Station (AMOS), the sponsor of this thesis. As background and motivation, this section will present an outline of the theory and principles of AMOS operations which are relevant to the problem of image quality measurement.

1.1.1 Imaging of Orbiting Satellites. AMOS is located atop Mt Haleakala on the island of Maui in the state of Hawaii. The station operates a 1.6 meter telescope used to obtain high resolution imagery of space objects, especially low earth orbit (LEO) satellites. [13].

Since AMOS is interested in *imaging* versus merely *tracking* a satellite, the resolving power of the telescope is all-important. A 1.6 meter telescope, in a vacuum, has a *diffraction limited* (or theoretical) resolution, θ , of about 0.08 arc seconds or about .39 microradians (if we use Rayleigh's criterion, $\theta = 1.22\lambda/D$ where λ is the wavelength of light being detected, say 500 nanometers, and D is the 1.6 meter diameter of the telescope). For a satellite 500 kilometers away from the telescope, this means that one could not expect to discriminate any feature smaller than 19 centimeters from any adjacent feature on the satellite.

The resolving power of the telescope is further limited by the intervening atmosphere between target and telescope. Due to the thermodynamics of the Earth, the atmosphere, and their interaction, the atmosphere is not thermally uniform and isotropic. Atmospheric turbulence in the line of sight of the telescope causes the index of refraction of the atmosphere to vary randomly at different points across the field of view of the telescope. This in turn leads to random phase and amplitude aberrations in the pupil of the telescope [5].

There are regions of relatively constant index of refraction at random positions in the field of view of the telescope, lasting for a random length of time (on the order of microseconds). The view is filled with these regions, known as *turbulent eddies*, and the statistics of the sizes and durations of these eddies have the effect of limiting the effective diameter (for resolving purposes) of the telescope. This effective diameter, known as the *Fried Parameter* or *atmospheric coherence diameter*, r_o , depends only upon atmospheric conditions, regardless of the physical diameter of the telescope [5]. At the AMOS location, r_o can typically vary from 5 to 12 centimeters.

Even though the telescope has an actual diameter of 1.6 meters, and can gather photons more effectively than a smaller telescope, with conventional optics it can only resolve space objects as well as an r_o -diameter telescope. Since r_o is an order of magnitude smaller than 1.6 meters (say 10 centimeters), the denominator of Rayleigh's resolution formula becomes smaller and θ becomes larger by the same factor. For our example satellite at 500 kilometers slant range, we can now only resolve objects on the order of a meter or more in size.

Another complicating factor is that LEO satellites move rapidly across the sky, so the target is constantly being viewed through different parts of the atmosphere and different sets of turbulent eddies, each with different statistical properties. Also, the aspect angle between the sun, satellite, and telescope is constantly changing, and, if the satellite is tumbling, spinning, or tracking the earth, it presents a constantly

changing aspect to the telescope. This limits the length of exposures, and limits the number of exposures which can be averaged together for post-processing [16] [18].

1.1.2 Hybrid Imaging. There is nothing that can be done about the translation and rotation of a target satellite. But there are two possible approaches to tackling the problem of atmosphere-induced aberrations when imaging space objects:

- the incoming distorted wavefront can be physically corrected by an *adaptive optics system*
- the raw telescope images can be *digitally reconstructed*

1.1.2.1 Adaptive Optics. An adaptive optics system (Figure 1.1) attempts to physically correct the phase aberrations induced by the atmosphere. It uses a wavefront sensor which measures the deformations that the wavefront has experienced while traveling through the atmosphere. The controlling computer uses this data to generate commands to the deformable mirror, which ideally should induce the exact conjugate of the phase aberrations in the wavefront, thereby removing the deformations, in real time.

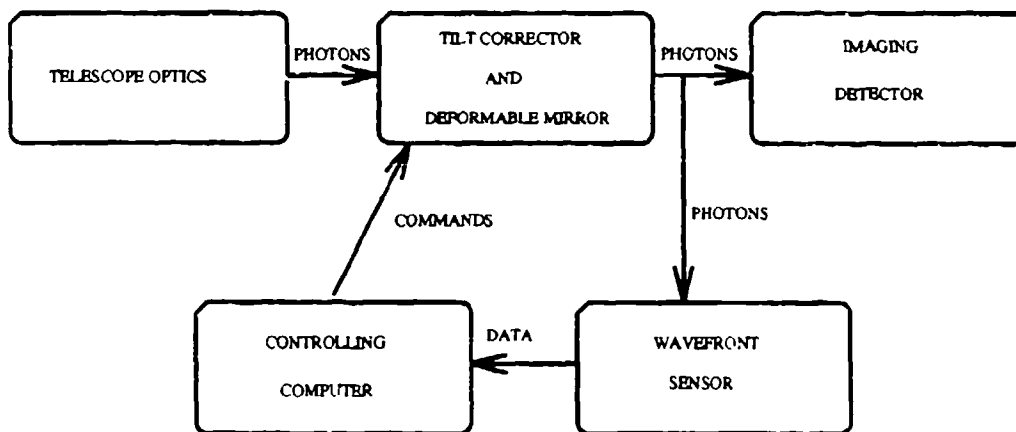


Figure 1.1 Adaptive Optics Concept

The AMOS Compensated Imaging System (CIS) (Figure 1.2) is a typical example of such a system [13]. The CIS consists of a closed-loop system with wavefront

sensor, wavefront computer, wavefront corrector, and image sensor. The wavefront sensor uses two shearing interferometers to measure the slope of the wavefront in two orthogonal directions at 152 discrete subaperture positions. The wavefront computer then uses these slope measurements to calculate the corrections necessary to remove the phase distortions.

The wavefront corrector consists of a tilt corrector mirror and a deformable, monolithic, piezoelectric mirror (DM) with 168 actuators [13]. The tilt corrector mirror uses commands from the wavefront computer to remove gross wavefront tilt error, "centroiding" the image (keeping it centered on the image plane). The DM actuators receive commands from the wavefront computer and deform the shape of the mirror to at least partially cancel out the estimated higher order errors. A slow-scan charge-coupled device (CCD) camera then captures the compensated image and records it on a computer disk and then digital tape for eventual digital processing and shipment to customers.

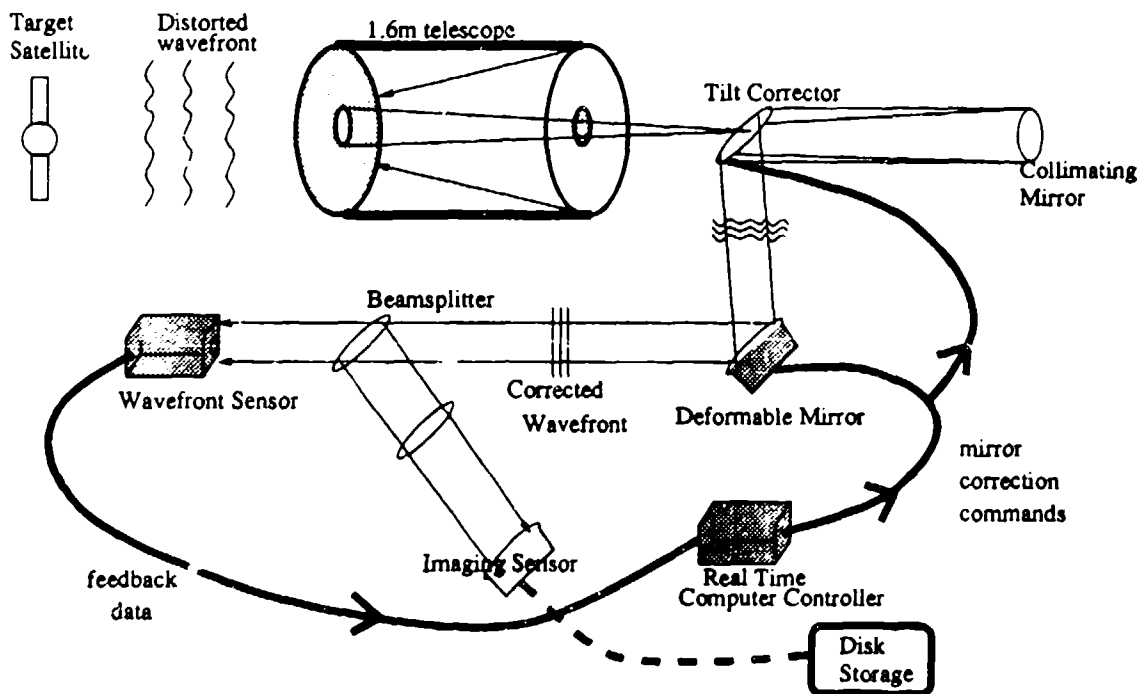


Figure 1.2 AMOS Compensated Imaging System

The adaptive optics reconstruction process does not provide perfect correction of an image. The adaptive optics process is limited in its effectiveness by:

- Spatial density of wavefront sensor subapertures
- Spatial density of deformable mirror actuators
- Errors and noise in wavefront sensor measurements (sensitive to low light levels)
- Time lag between wavefront sensor measurements and deformable mirror actuation
- Amplitude perturbations, which cannot be corrected [1]
- Errors in telescope construction such as fixed aberrations, optical misalignment, and actuator misplacement.

These facts leads one to consider supplementing the adaptive optics process with image reconstruction via digital post-processing. ¹

1.1.2.2 Digital Image Reconstruction. Optical imaging with discrete detectors can readily be treated as a two-dimensional linear systems/discrete signal processing problem. Linear, shift-invariant systems are completely characterized by

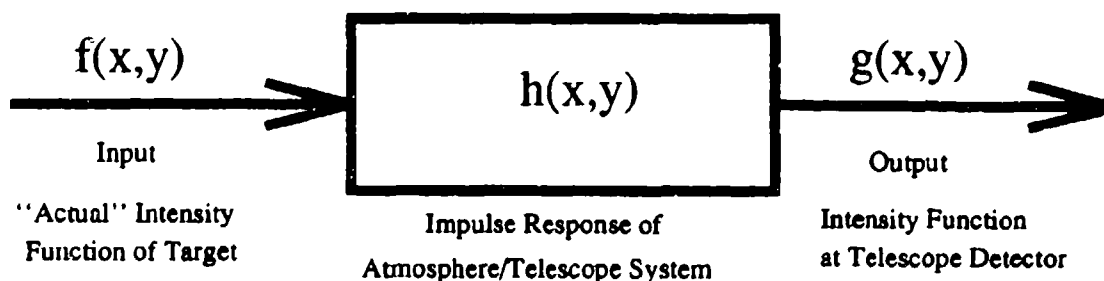


Figure 1.3 Linear System Model

their impulse response or point spread function (PSF) $h(x,y)$. The output of such

¹Some terminology: an adaptive optics system that has less than one WFS subaperture and DM actuator pair per atmospheric coherence diameter r_0 , such as the AMOS CIS, is said to be *partially compensated*.

systems, $g(x, y)$, is related to the input, $f(x, y)$, by the *convolution sum* [6]:

$$g(x, y) = \sum_i \sum_j f(i, j)h(x - i, y - j) = f(x, y) * h(x, y), \quad (1.1)$$

and also by the Fourier Transform ² frequency domain *filtering property* or *convolution theorem*:

$$(g(x, y) = f(x, y) * h(x, y)) \iff (G(u, v) = F(u, v)H(u, v)), \quad (1.4)$$

where the asterisk denotes convolution and " \iff " denotes a Fourier Transform pair. The following terminology is adopted.

- $H(u, v) \implies$ Optical Transfer Function (OTF)
- $|H(u, v)| \implies$ Modulation Transfer Function (MTF)
- $G(u, v) \implies$ Image Spectrum
- $|G(u, v)| \implies$ Magnitude Spectrum
- $|G(u, v)|^2 \implies$ Spectral Density.

Note that in this formulation the frequency variables refer to spatial frequency, and high spatial frequency generally corresponds rapid changes in image gray levels spatially across the image. This in turn often corresponds to the highly resolved features of the image.

²The 2-Dimensional Discrete Fourier Transform is:

$$F(u, v) = \frac{1}{N} \sum_{x=0}^{N-1} \sum_{y=0}^{N-1} f(x, y) \exp\left(\frac{-j2\pi(ux + vy)}{N}\right) \quad [6] \quad (1.2)$$

(for square arrays), and its inverse becomes

$$f(x, y) = \frac{1}{N} \sum_{u=0}^{N-1} \sum_{v=0}^{N-1} F(u, v) \exp\left(\frac{+j2\pi(ux + vy)}{N}\right). \quad (1.3)$$

u and v are *spatial frequency* variables.

The imaging process can be viewed as a linear system. The actual intensity function $f(x, y)$ of the target satellite can be viewed as the input. The intensity function at the image plane of the telescope (as sampled by the detectors) is the output $g(x, y)$. The diffraction effects of the telescope and the "degradation" effects of the atmosphere are characterized by a point-spread function, $h(x, y)$.

If we knew the PSF of the imaging process, $h(x, y)$, we could ideally find the original target $f(x, y)$ by $F(u, v) = \frac{G(u, v)}{H(u, v)}$. This concept is known as *inverse filtering*. There are three problems with this simple approach:

1. If $H(u, v)$ approaches zero at any point the calculated $F(u, v)$ would be theoretically unbounded and numerically wrong, a manifestation of the fact that there is no information available from the spatial frequencies where $H(u, v) = 0$.
2. Random noise is always introduced in the detection process, adding uncertainty to the measurement of $g(x, y)$ (See Figure 1.4).
3. The OTF is actually a random variable, changing with time, because of noise and the constantly changing atmospheric turbulence. The best that can be hoped for is knowledge of the statistics of the OTF.

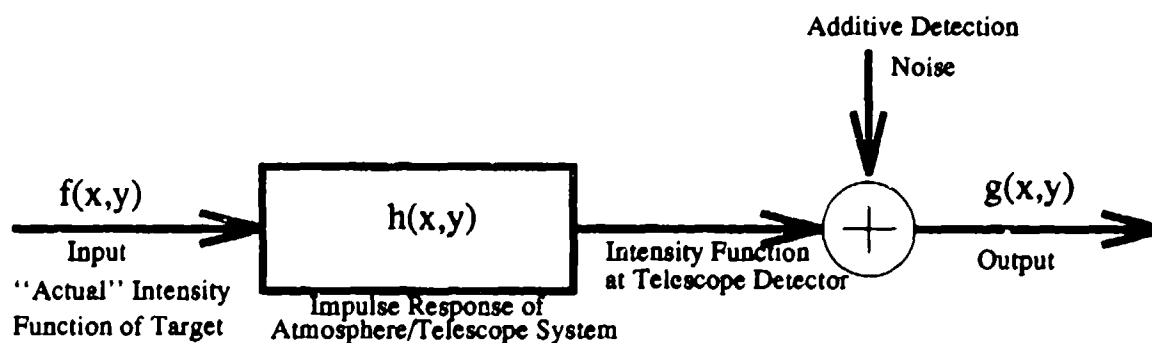


Figure 1.4 Linear System Model With Detection Noise

Problems with noise and amplitude aberrations can be partially overcome by averaging large numbers of short exposures together. Intuitively this makes some sense since a sudden random change (i.e. noise) in one sample of a random variable

would be partially averaged out by other samples taken at different times. The net effect would be a "smoothing" of noise effects. An estimate of $F(u, v)$ can be obtained by $\hat{F}(u, v) = \frac{\langle G(u, v) \rangle}{\langle H(u, v) \rangle}$ where $\langle \dots \rangle$ denotes ensemble averaging. An example ensemble-averaged satellite image³, or $\langle g(x, y) \rangle$, is shown in Figure 1.5. The magnitude of the



Figure 1.5 Ensemble-Averaged Satellite Image

Fourier Transform of this image, or magnitude spectrum, is shown in Figure 1.6.

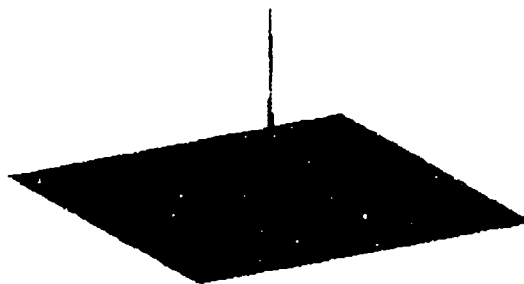


Figure 1.6 Modulus of FFT of Satellite Image

³Since AMOS images are captured on a two-dimensional CCD array, it is customary to view an image as a two-dimensional array of gray levels. AMOS images are generally processed as 128 by 128 matrices of gray levels with 14 bit quantization. In other words, the minimum element (0) is black and the maximum element (16383) is white, with integer gray levels linearly scaled in between these two extremes. The value of a gray level corresponds to a measured integrated average intensity at a corresponding area in the image plane of the telescope.

An estimate of the impulse response (PSF) of the imaging process is also sought. In optical signal processing, a point source of light can serve as an impulse function. The sky is full of stars which serve as excellent point sources. An ensemble average of images of a star taken immediately before or after a target satellite pass provides $\langle h(x,y) \rangle$, an estimate of the PSF. See Figure 1.7 for an example. Taking



Figure 1.7 Ensemble-Averaged Star Image (Point Spread Function Estimate)

the Fourier Transform of the average PSF gives us the average OTF of the imaging process (estimated) [5]. See Figure 1.8. The origin is in the center of the 2-D surface plot.

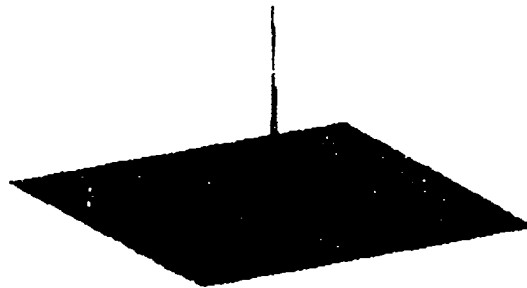


Figure 1.8 Magnitude of the Ensemble-Averaged OTF

The satellite FFT is divided by the OTF estimate above. This has the effect of amplifying the higher spatial frequencies of the satellite image. Notice, however, that

the OTF gets smaller with increasing spatial frequencies. While it is true that the presence of Fourier coefficients at higher spatial frequencies generally implies higher resolution, the telescope has a fundamental limit on its resolution. Therefore, it is *band-limited* in the Fourier domain. Any Fourier coefficients beyond this frequency can only be the result of noise since this information could not have possibly been captured by the band-limited telescope system.

The higher spatial frequencies of the telescope passband contain valid image information, but also contain noise energy as well. Consider, for example, if the OTF, $H(u, v)$, is known exactly, but $G(u, v)$ is detected in the presence of additive noise. Applying the inverse filtering relation, $\hat{F}(u, v) = \frac{G(u, v)}{H(u, v)}$ this equation would reduce to $\hat{F}(u, v) = F(u, v) + \frac{N(u, v)}{H(u, v)}$ where $N(u, v)$ is the image noise spectrum. If the OTF ever approaches zero in the telescope passband, which it does (Figure 1.8), the $\frac{N(u, v)}{H(u, v)}$ term would take on large values and amplify the noise in the image.

It is reasonable to suppose that if a second filter is applied, one which attenuates the effects of these noise-dominated higher frequencies, acceptable results might be obtained. AMOS personnel prefer a triangular cross-section (conical) lowpass filter

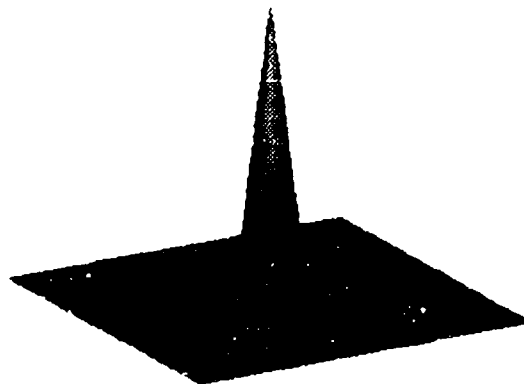


Figure 1.9 Inverse Filtering Noise Filter

for reconstruction noise attenuation [18] (Figure 1.9). This modified approach to inverse filtering is commonly used for reconstructing AMOS images. The spectrum of the inverse filtered, triangle filtered example image is shown in Figure 1.10. Compare this spectrum to the original ensemble image spectrum (Figure 1.6). Note that the new inverse filtered spectrum has energy content in the higher spatial frequencies. The inverse Fourier Transform of this spectrum is shown in Figure 1.11. Compare this reconstructed image to the original ensemble in Figure 1.5

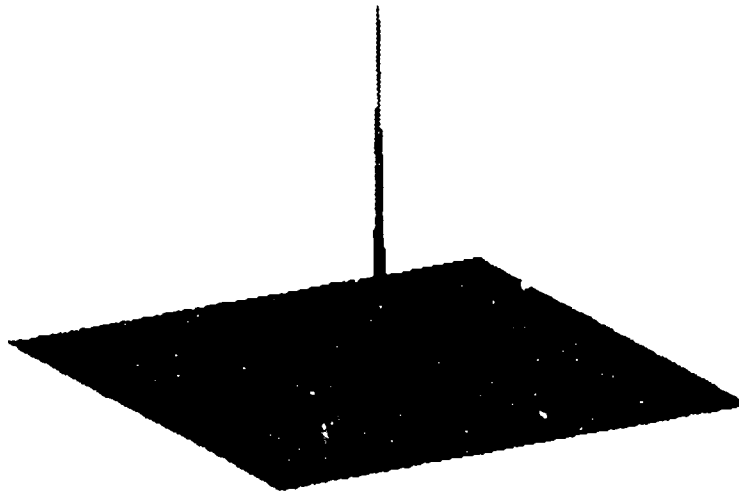


Figure 1.10 Reconstructed Image Spectrum



Figure 1.11 Reconstructed Satellite Image

1.2 *The Image Quality Problem*

It is generally accepted that the ultimate arbiter of image quality is the subjective opinion of the user of an image. This fundamental axiom implies several problems for the automatic processing of large amounts of AMOS digital imagery:

- *Ensemble Sifting*

During a particular AMOS satellite imaging session, hundreds of raw image frames are ingested into the postprocessing system for reconstruction. Experience has shown that some image frames are of noticeably poorer quality than others in the ensemble [22]. It may be desirable to exclude these lower quality images from the reconstruction ensemble [21].

- *Reconstructed Image Selection*

Recall the triangular cross-section noise filter of the modified inverse filtering reconstruction method. The optimum width that this filter should have is not readily apparent. The actual bandwidth of the optical system is changing randomly with r_o and the performance of the adaptive optics system. If the filter is too wide, noise will be let in which will detract from the image restoration goal. If the filter is too narrow, legitimate resolution detail from the target satellite will be excluded from the final product. Which filter width should be used? Also, several reconstructed images are produced during one observing session. The customer usually requires only a subset of these images.

These two classes of problems could be handled in an un-supervised fashion if some sort of "quality number" could automatically be assigned to the images. This number could be thresholded for rejection or acceptance of images, based on quality.

1.3 *Research Objective*

The goal of this research is to find a way to objectively and automatically measure the quality of an AMOS digital satellite image. This research will inves-

tigate if there exist certain quantities which can be extracted from digital images of space objects that correlate with perceived image quality. These parameters will be obtained using the Interactive Data Language (IDL), a commercially available data processing software package which is used to process imagery operationally by the thesis sponsors at AMOS [14] [15]. Any of these parameters which prove to be successful may eventually be integrated into AMOS operational image processing software wherever some indication of relative image quality is required.

1.4 Scope

This thesis deals with quantitative post-processing algorithms for monochrome digital images of extended objects against "dark" backgrounds, as gathered by an adaptive optics system similar in concept to the AMOS system. The actual performance and design of the adaptive optics system is not treated here. Advanced applications of Artificial Intelligence, Pattern Recognition, Neural Networks and other advanced computer science techniques are not treated here. Due to the security classification of the bulk of AMOS imagery, experimentation was limited to unclassified, simulated imagery (see Chapter 3). Subjective evaluation of imagery by experienced Photo-Interpreters is beyond the scope of this thesis.

1.5 Summary of Key Results

This research supports the hypothesis that automatic objective image quality measurement is possible for digital images of space objects. The two recommended image quality metrics (IQMs) presented here are

$$IQM = \sum_{\theta} \sum_{\rho=\rho_{lower}}^{\rho_{upper}} |F(\rho, \theta)| \quad (1.5)$$

and

$$IQM = var\{f_{sobel}(x, y)\} \quad (1.6)$$

where $F(\rho, \theta)$ is the discrete Fourier Transform of an image, ρ_{lower} and ρ_{upper} are the practical band limits of the human visual system, $f_{sobel}(x, y)$ is a Sobel edge enhanced image and $var[\dots]$ is sample variance. These algorithms were implemented in the IDL software package.

The metrics were tested and validated against a database of raw images generated by a software simulation of an atmospheric imaging adaptive optics system. Since the simulator allows precise control (and knowledge) of seeing conditions and target brightness, which directly impact image quality, changes in image quality metric values could be directly and objectively compared to changes in these simulation parameters. As simulated brightness or seeing conditions were quantitatively improved, a successful IQM should give a quantitatively higher image quality rating.

Also, recall that the modified inverse filtering operation discussed above requires the user to select the optimal noise suppression filter width. The image quality metrics were tested against a database of images reconstructed with a variety of noise suppression filter widths to give some indication of the feasibility of using these metrics for totally un-supervised image reconstruction.

In all test cases the metrics performed consistently, detecting absolute changes in image quality simulation parameters and noise filter widths. An operational evaluation of metric performance was not performed in this research. Such evaluation would necessarily include comparing photo-interpreter assessment to automated image quality metric rating, on actual imagery instead of simulated imagery.

1.6 Document Organization

Chapter 2 will discuss the current knowledge concerning un-supervised objective image quality assessment as found in the image processing and optics literature, and present the candidate Image Quality Metrics that were successfully tested.

Chapter 3 will discuss how the Image Quality Metrics were tested on "raw" image ensembles using simulation software.

Chapter 4 will discuss the results of the testing. A feasibility argument is also presented regarding the use of the Image Quality Metrics to automatically select the optimum width of the triangular reconstruction noise filter, mentioned previously in this chapter.

Chapter 5 will discuss conclusions and any further research that may be indicated.

II. Image Quality Metrics

Since the goal of this research is measuring relative image quality, a reasonable first step would be to obtain two different quality images of the same object and compare and contrast various quantities associated with the images. If there are any differences found, the next step would be to determine if these differences appear consistently for all images of different quality, and then determine if this effect is consistent for a variety of different targets. Choosing quantities to be tested is the subject of this chapter, and the testing of those quantities is covered in Chapters 3 and 4.

In the image processing literature, images are generally analyzed in the spatial domain (i.e. analysis of characteristics and distribution of the actual pixels) or in some transform domain, where the image is represented as the coefficients of some linear combination of orthogonal basis functions (or basis images) [6]. Section 1 discusses image quality measurement with the most commonly used of these transforms, the Fourier Transform, mentioned in Chapter 1. Section 2 discusses Image Quality Metrics derived from spatial domain quantities of the image.

2.1 The Fourier Transform and Image Quality

In Chapter 1 the Linear Systems/Fourier Optics model of image propagation was discussed. It was mentioned in passing that the u and v frequency variables are *spatial* frequency variables. This implies that the higher the spatial frequency, the faster things are changing in the image. This alone might intuitively lead one to think that a "good" (i.e. highly resolved, good detail) image could have a larger amount of spectral content in the higher spatial frequencies than a "bad" image, since "detail" implies that gray levels are changing rapidly across the image as the structure of the target is revealed [3].

Also, spectral content in the very low frequencies would generally imply simple, large-area changes in background level [3]. Therefore, the very low spatial frequencies might not have a serious impact on the amount of target detail that an image reveals.

The working hypothesis in this section is that "good" image spectra differ in some quantifiable and consistent manner from "bad" image spectra. The intuitive arguments presented above lead to the specific hypothesis that

$$(\text{high frequency spectral content}) \iff (\text{"good" image}). \quad (2.1)$$

If this hypothesis can be supported, then an Image Quality Metric (IQM) such as:

$$\int_0^{2\pi} \int_{\rho_{lower}}^{\rho_{upper}} |F(\rho, \theta)| d\rho d\theta \quad (2.2)$$

is implied (F is the image Fourier Transform discussed in Chapter 1, where u and v Cartesian frequency coordinates have been changed to ρ and θ polar frequency coordinates, $\rho = \sqrt{u^2 + v^2}$ or the Euclidean distance from zero frequency). There is support in the literature for such a hypothesis, as discussed next.

2.1.1 Human Visual System Transfer Function. The idea that the human visual system (HVS) is more receptive to some spatial frequencies and less receptive to others, as implied above, is widely accepted [6] and can be readily translated into a linear systems vocabulary. Specifically, the underlying hypothesis is that the HVS can be modelled as a spatial frequency transfer function [10] [11] [12] [19].

Under certain simplifying assumptions¹, a relatively simple first order approximation of the Human Visual System as a magnitude transfer function (MTF) has been developed. The relevant research involved experimentation with human observers who evaluated images with periodic patterns of different fundamental fre-

¹Assumptions such as: the gray level differences are limited to the approximately linear portion of HVS dynamic range; the observer can look at the image for as long as is preferred; the observer is at the optimal distance from the image representation.

quencies. By noting the observers' sensitivity across a variety of spatial frequencies, an approximation to the frequency response of the HVS could be estimated [11].

The researchers found that the HVS is insensitive to all but gross changes at very low spatial frequencies. Also, like all optical systems, the HVS is band-limited, and insensitive to higher frequency structure in an image. (Note that there would also be bandwidth constraints imposed by the optics and sampling of the imaging system.) Taken together, the conclusion is that the HVS transfer function can be approximated as a rotationally symmetric bandpass system, with one possible cross section shown in Figure 2.1. Analytical fits to this curve such as:

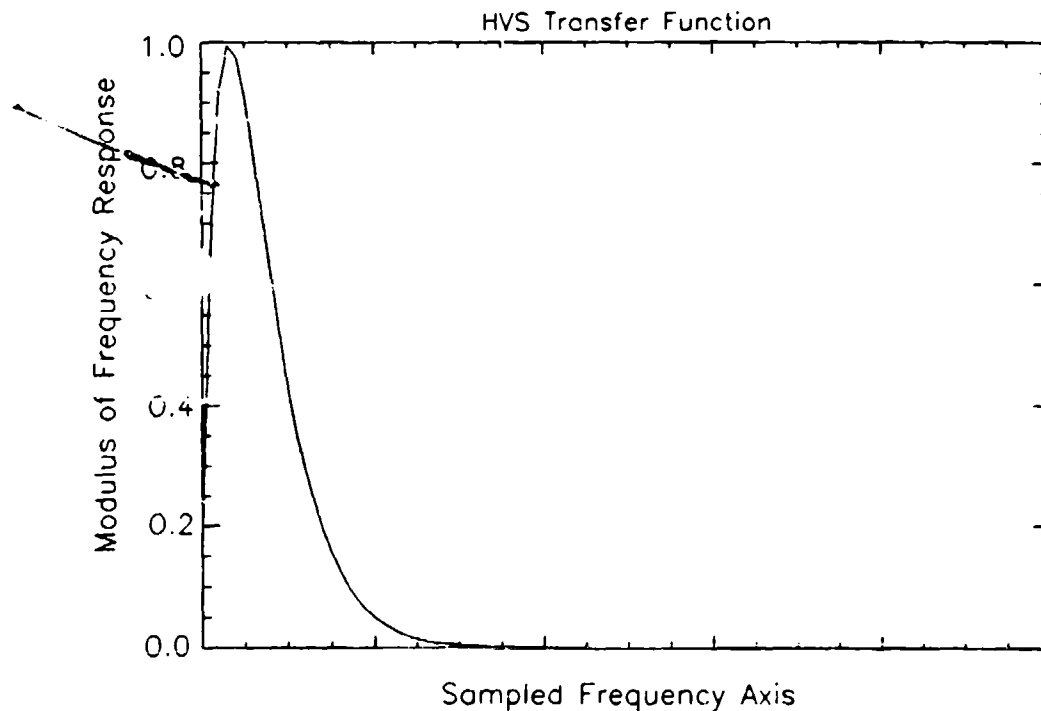


Figure 2.1 Frequency Response of HVS

$$|H(\rho)| = (A + B\rho)e^{C\rho} \quad (2.3)$$

are often used, where A,B,and C are determined empirically for each application, and depend on image display, observer distance from display, image sampling and

array size [11]. This idea that the HVS can be modelled as a bandpass filter will feature prominently in the effort to measure image quality, as discussed next.

2.1.2 Spectral Image Quality Metric. How can this model be applied to image quality measurement? Observe the two images of a Russian Okean satellite shown in Figure 2.2. These images were obtained from an adaptive optics simulation



Figure 2.2 Okean Satellite, $r_o = 5$ (left) and 15 (right) cm respectively

described in Chapter 3. The imaging conditions are alike in every respect except seeing conditions: $r_o = 5$ cm on the left and 15 cm on the right. It is clear that the second image reveals more detail about the target.

How do the spectra of the two images compare? First of all, to make a meaningful comparison, the energy of the two images must be normalized:

$$f_{norm}(x, y) = \frac{f_{orig}(x, y)}{\sum_x \sum_y f_{orig}(x, y)} \quad (2.4)$$

where $f_{orig}(x, y)$ is the original image. Also, since depicting the comparison of 2 two-dimensional surface plots is difficult, it would be convenient (at least for the purpose of presenting the concepts) to radially average the modulus the two spectra:

$$F_{radavg}(\rho) = \frac{\sum_{\theta} |F(\rho, \theta)|}{\text{number of pixels at distance } \rho} \quad (2.5)$$

where $|F(\rho, \theta)|$ is the modulus of the discrete two-dimensional Fourier Transform of $f_{norm}(x, y)$ (again in polar coordinates with $\rho = \sqrt{u^2 + v^2}$, the Euclidean distance

in pixels - rounded to the nearest integer - from the zero frequency origin). Now $F_{radavg}(\rho)$ is a real one-dimensional array which can be plotted as a curve instead of a surface.

The radially-averaged spectra of the two example images are shown in Figure 2.3. Note that the curve corresponding to the good image spectrum is greater than the curve corresponding to the bad image spectrum for a specific midrange band of frequencies. Chapter 4 will show that this effect occurs consistently for a wide variety

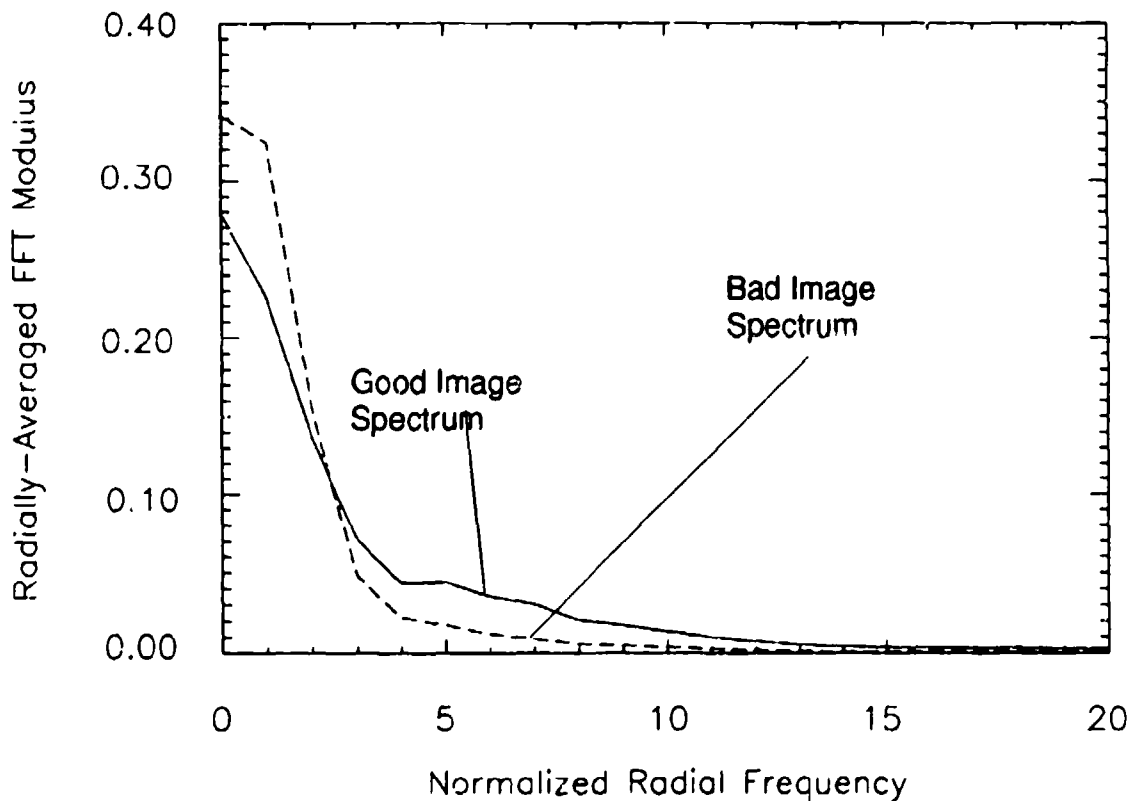


Figure 2.3 Spectral Comparison of Different Quality Images

of targets and image degradation effects tested in this research, a vitally important result. The same result is documented in [10]. This result is consistent with our model of the HVS as a bandpass system, since:

- the AMOS mission involves the high *resolution* imaging of space objects for consumption by human analysts;
- the Fried Parameter r_o is a direct indication of the quality (resolution) of an AMOS image for this application.

Therefore a larger- r_o image should have higher frequency content in the HVS band-pass frequencies.

Since the the area (or volume in the non-radially averaged spectrum) under the curve is different for images of different quality (within a certain frequency range), the following candidate spectral Image Quality Metric (IQM) is suggested:

$$IQM = \sum_{\theta} \sum_{\rho=\rho_{lower}}^{\rho_{upper}} |F(\rho, \theta)| \quad (2.6)$$

where the ρ_{lower} and ρ_{upper} are determined empirically. The selection of these limits will be discussed in Chapter 4. Note that this formulation is in effect integrating (summing) the magnitude spectrum after filtering by a rectangular cross-section bandpass filter. This rectangular bandpass filter could be regarded as a simpler approximation of the HVS bandpass shown in Figure 2.1.

A similar quantity to the above IQM is suggested in [12]. The major difference there is that instead of using the rectangular filter approximation as above, the image is filtered with an analytical curve-fit of Figure 2.1 as well as a filter to deal with oblique-angle effects in aerial remote sensing (which doesn't apply to this thesis).

The Interactive Data Language (IDL) software package implements the so-called "Fast" Fourier Transform (FFT) algorithms, facilitating easy implementation of this metric. This metric was tested (see Chapter 3) and its performance is discussed in Chapter 4.

2.2 Histograms and Image Quality

The histogram of an image is a common spatial domain image processing and analysis tool. The histogram of an image is simply a tally of the number of picture elements (pixels) that have a certain gray level, plotted against gray level: $histogram = n(k)$ where $n(k)$ is the number of pixels with *gray level* = k . The histogram bin sizes are generally the same as the gray-level quantization of the imaging system, making the histogram a discrete array of integers. Normalizing the curve $n(k)$ to unit area yields a first order estimate of the *probability density function* (PDF) of the image: $p(k) = \frac{n(k)}{N^2}$ (for $N \times N$ array) [6] [4].

The working hypothesis here is that images of different quality have consistent, quantifiable differences in their histograms.

2.2.1 Histogram-Based Image Quality Metrics. Consider again the two satellite images in Figure 2.2. After normalizing the energy of the first image to be the same as the second image², or

$$A = \sum_x \sum_y f_1(x, y) \quad (2.7)$$

$$B = \sum_x \sum_y f_2(x, y) \quad (2.8)$$

$$f_{1, norm}(x, y) = \frac{B f_1(x, y)}{A} \quad (2.9)$$

(where $f_{1,2}(x, y)$ are the respective images in Figure 2.2) the histograms of both of these images are calculated (Figures 2.4).

A distinct difference in the shape of the histogram curves is evident. Observe, for example, that the good image histogram has entries at the higher gray levels, while the bad image histogram does not. This indicates that, even though both

²This allows energy normalization, while keeping convenient integer histogram bin sizes, as opposed to normalizing to unit energy, where all gray levels and bin sizes would be fractional.

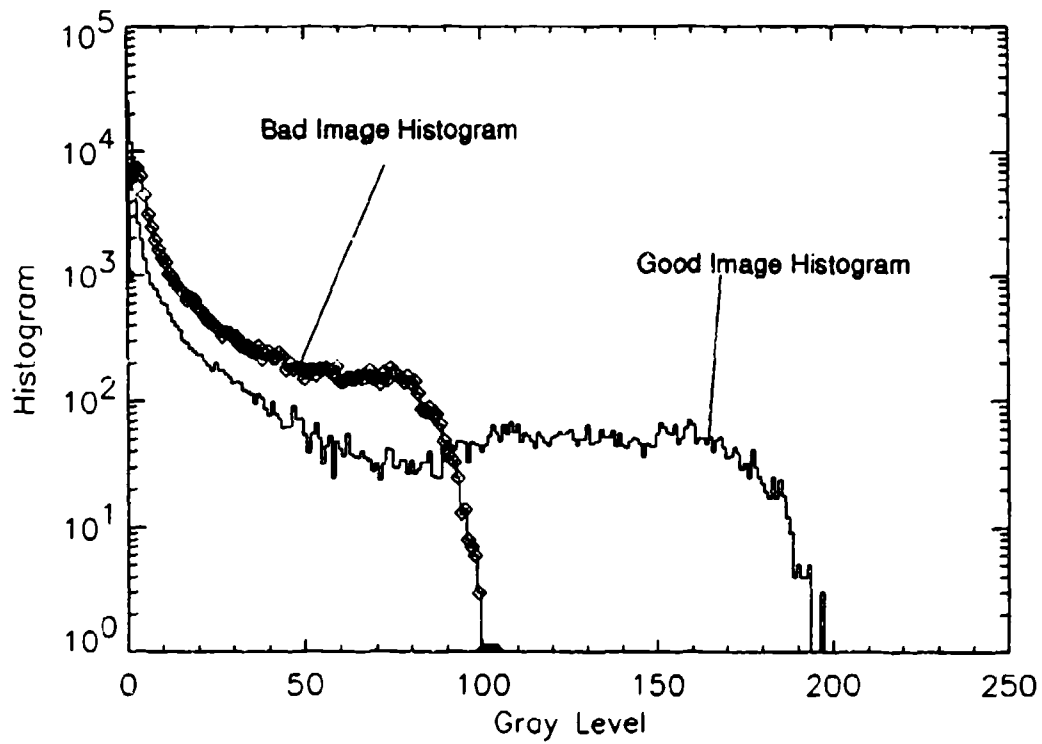


Figure 2.4 Histograms of Good and Bad Images, (normalized to the same energy)

images have the same total energy, the better image has some brighter pixels. Also note that the better image has more zero pixels. This is because the bad image, which is of poorer resolution, has its image energy "smeared out" across the image, yielding non-zero (gray) pixels in the worse image that were (zero) black in the better image.

2.2.1.1 Histogram Features and Image Quality. The above observations are all somewhat subjective. The goal is to somehow extract parameters from these histograms that captures these observations in a way that correlates with image quality. As a starting point, note the following common parameters, called *histogram features*, which are often used to characterize image histograms [6]:

HISTOGRAM PARAMETERS:	
Moments	$m_i = \sum_{k=0}^{g_{max}} k^i p(k)$
Absolute Moments	$\hat{m}_i = \sum_{k=0}^{g_{max}} k ^i p(k)$
Central Moments	$\mu_i = \sum_{k=0}^{g_{max}} (k - m_1)^i p(k)$
Absolute Central Moments	$\hat{\mu}_i = \sum_{k=0}^{g_{max}} k - m_1 ^i p(k)$
Entropy	$H = - \sum_{k=0}^{g_{max}} p(k) \log_2 p(k)$

where g_{max} is the maximum gray level in the histogram. These quantities are not unique to image processing, but are also used in general statistics applications. As such, some of these parameters are better known by other names:

first absolute central moment, $\hat{\mu}_1$	dispersion
second central moment, μ_2	variance
second moment, m_2	mean square value
third central moment, μ_3	skewness
fourth central moment, μ_4	kurtosis

Note that some of these features can be measured without explicitly determining the histogram:

$$m_i = \sum_x \sum_y f^i(x, y) \quad (2.10)$$

$$\mu_i = \sum_x \sum_y (f(x, y) - m_1)^i \quad (2.11)$$

$$\hat{\mu}_i = \sum_x \sum_y |f(x, y) - m_1|^i \quad (2.12)$$

Consider again the two example histogram curves. Obviously, the shapes of the curves are significantly different. It is plausible that the moments of these curves can provide a quantitative indication of the aspects of histogram shape that may be relevant to image quality. Variance, for example, as mentioned in [6] can give an indication of "activity", in the gray level amplitudes. This is the same intuitive argument mentioned in the previous section of this chapter as a motivation to investigate spatial frequency quality metrics. The working hypothesis here is that some or all of these histogram features correlate with AMOS image quality.

2.2.2 Histogram Features as Structure Factors. Linfoot [8] presents similar intuitive arguments when he redefines some of the above histogram features as follows for an energy normalized image:

second moment, m_2	structural density factor
variance, μ_2	normalized mean structural density
dispersion, $\hat{\mu}_1$	$\int_{x,y} c(x, y) dx dy$ <p>such that $c(x, y) = \text{"structure function" or "contrast function"}$ $= f(x, y) - m_1$</p>

He relates these factors to the "peakiness" or variability of image amplitudes, and the amount of structure or "fine object detail" an image contains. Thus, support for the hypothesis exists in optics literature.

2.2.3 Histogram Features as Sharpness Functions. Buffington and Muller [2] also present some of the histogram features given above, but from an entirely different context, using an idea they call *image sharpness*. The authors' goal was to derive algorithms (called sharpness functions) that produce a maximum output

when phase distortion at the telescope image plane is at a minimum. Their eventual goal is to use image "sharpness" measurements to drive adaptive optics hardware in a feedback loop, providing real-time maximization of the sharpness function, and therefore, real-time correction of image phase distortion.

Consider one sharpness function given in [2]:

$$S_3 = \int \int_{image} M(x, y) f(x, y) dx dy \quad (2.13)$$

where $f(x, y)$ is the received image and $M(x, y)$ is the target image, known *a priori*. Now, since it assumes prior knowledge of the target, it cannot be used operationally at AMOS, but it is instructive to consider it for illustration purposes.

The sharpness function above is similar to the *correlator/matched-filter* concept in digital communication theory. Consider a digital communications receiver which receives a waveform that has been corrupted by noise or other propagation effects. The receiver's purpose is to find out which symbol was sent. One common approach is to cross-correlate the received waveform with a collection of stored symbols, and select the symbol that gave the highest cross-correlation value³. Buffington and Muller are using nearly the same concept in their scheme of image correction.

Now, if the target is not known *a priori* (e.g. AMOS operations), then the target function $M(x, y)$ in S_3 can be replaced with $f(x, y)$, the received image, as in the Buffington-Muller sharpness function given by

$$S_1 = \int \int_{image} f(x, y) f(x, y) dx dy \quad (2.14)$$

or

$$S_1 = \int \int_{image} f^2(x, y) dx dy \quad (2.15)$$

³For two real one-dimensional functions $f(x)$ and $M(x)$, cross-correlation is defined as $r_{fM}(x) = \int_{\alpha} f(\alpha) M(x + \alpha) d\alpha$ and the autocorrelation of $f(x)$ is defined as $r_{ff}(x) = \int_{\alpha} f(\alpha) f(x + \alpha) d\alpha$.

which is the second moment, and also the autocorrelation peak $r_{ff}(0,0)$, of the image. Buffington and Muller prove that this function is also maximized when telescope phase aberration is minimized. Similar conclusions are reached for the third and fourth moment functions.

Three different arguments have now been cited as motivation for investigating various statistical moments of an image with respect to image quality. Of all the moments mentioned above, only the second central moment will be given further consideration here. This is due to its intuitive connection to the idea of variance, where variance of image amplitudes generally imparts image information. Preliminary testing early in this research effort concluded that the first, third and fourth moment performed nearly the same as variance regarding the relative measurement of image quality.

Also note that there is no real basis, other than convenience, for choosing between the second moment (sharpness) and the second central moment (variance) as a measure of relative image quality when the images have been energy-normalized. This is because $var[f] = E[f^2] - (E[f])^2$ (where $var[\dots]$ is the variance operation and $E[\dots]$ is the expectation operation) and if the image f is always normalized to the same value, $E[f]$ and therefore $(E[f])^2$ will always be the same value, so the variance and sharpness will always differ by the same constant. Image sample variance is therefore arbitrarily chosen here for further investigation as an image quality metric.

2.2.4 Histogram Features, Information Theory, and Entropy. Entropy is an important concept in many areas of digital signal processing, and since it is often intuitively related to the information content of a signal, it is a natural choice for a candidate image quality metric. As will be seen in Chapter 4 however, it did not prove to be a consistent indicator of image quality. As a rule, unsuccessful image quality metrics are not discussed in this thesis, but it was felt that entropy is an

important enough quantity that its testing and failure in this research effort should be explicitly noted.

Entropy, as originally introduced in the field of statistical mechanics, is a measure of the number of microscopic states by which a given macroscopic state can be realized. If there are N possible, equally likely microscopic states, the entropy is given by

$$H = \ln N = -\ln \frac{1}{N} = -\ln p \quad (2.16)$$

where p would be the probability of each state. If the states are not equally likely, but each have probability $p(k)$, then the entropy is an average [9]:

$$\langle -\ln p(k) \rangle = -\sum_k p(k) \ln p(k). \quad (2.17)$$

Shannon provided the mathematical basis for modern communications theory when he applied the entropy concept to messages and information, replacing thermodynamic micro-states with message symbols [20]. In this formulation, information imparted by a symbol in a message depends on the number and probability of each particular symbol. For image processing applications, the gray level of a pixel plays the role of a symbol. Typically, in information theory applications to digital data, the above natural logarithm is usually replaced by \log_2 which is accomplished by simply dividing by $\ln 2$. [20]

Consider a 256 X 256 pixel eight bit image, where there are 65536 elements which can each take on 256 values. If the pixels were all the same value, the image would convey little information, since, practically speaking, there would be no image. Only one bit of information per symbol, versus 8 ($2^8 = 256$ gray levels), would be needed to convey the information in the image. An image with 8 gray levels could reveal quite a bit more detail about different brightnesses at different parts of the target. This image might require at least three bits per symbol ($2^3 = 8$ gray levels) to convey the information in the image. The trend that these examples are meant to

show here is that an image with more “information content”, or entropy, has a wider and flatter histogram. In fact, entropy is maximized for a “flat” or uniform PDF, or histogram. More generally, entropy provides some measure of histogram shape. Also, since entropy gives a quantitative indication of the “uncertainty” of a message there an intuitive argument for investigating entropy as an Image Quality Metric.

2.2.5 *Histogram-Based Image Quality Metrics with Spatial Filtering.* Consider the second moment image quality metric mentioned previously:

$$S_1 = \int \int_{\text{image}} f^2(x, y) dx dy = r_{ff}(0, 0) \quad (2.18)$$

By Parseval’s Theorem this quantity is equal to

$$\int_u \int_v |F(u, v)|^2 du dv \quad (2.19)$$

or in discrete form:

$$\sum_u \sum_v |F(u, v)|^2. \quad (2.20)$$

This expression is similar in concept to the spectral image quality metric from the first section of this chapter:

$$IQM = \sum_{\theta} \sum_{\rho=\rho_{\text{lower}}}^{\rho_{\text{upper}}} |F(\rho, \theta)|. \quad (2.21)$$

In both cases the two preceding equations are adding the modulus (or modulus squared) of Fourier coefficients of an image.

Notice however, that the second moment is the sum of all image energy regardless of spatial frequency. This ignores the idea presented previously that energy in very low spatial frequencies is relatively unimportant to image quality. This leads to the following question: given that the human visual system (HVS) acts as a band-pass filter, would it be desirable (and possible) to also “filter” the images in the

spatial domain before applying the histogram/image moment-based IQMs, as was done with the spectral IQM?

Part of the answer to this question lies in the fact that histograms (and image moments derived from them) contain no pixel position information. One could take a nearly perfect image of the highest quality and randomly rearrange the pixels into a meaningless jumble and the histogram and the IQMs based on it would remain unchanged. Another aspect to consider is that noise manifests itself as random variations in image pixel values. The worst-case scenario is that one of the candidate spatial IQMs could possibly indicate that an image with high noise was of *higher* quality than an image with low noise, just the opposite of what is desired.

It is possible to approximate the effect of a frequency-domain filter in the spatial domain. This is known as *spatial filtering*. The basic approach is to replace a pixel value with some linear combination of the value of itself and its neighbors. This can be visualized as sliding a mask: (Figure 2.5) across the image and replacing

W1	W2	W3
W4	W5	W6
W7	W8	W9

Figure 2.5 Spatial Filter General Mask

the pixel at the center of the mask with, for example, the sum of the products of the mask values and the pixel values under the mask. In Figure 2.5, for example, if the values of the pixels under the mask are p_1, p_2, \dots, p_9 , then the pixel p_5 becomes $p_{5,new} = w_1p_1 + w_2p_2 + \dots + w_9p_9$. Note that pixel position information now plays a factor in the new, spatially-filtered image. Note also that the Fourier Transform of

the image is not needed to perform the filtering, implying a significant computational savings in most cases [4].

One of the most important categories of spatial filters are known as *edge detection operators* [4]. The mask of the Sobel edge detection operator is shown in Figure 2.6. These two masks are both applied to the image, one after the other.

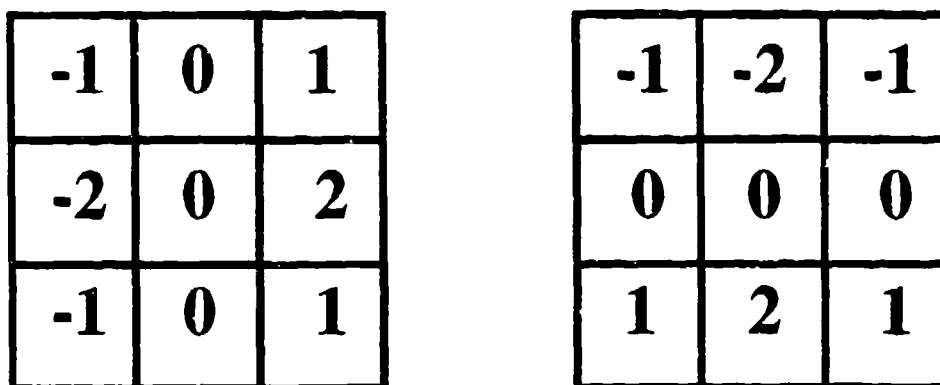


Figure 2.6 Sobel Operator Masks

There are two masks because of the nature of the *gradient* operation upon which the Sobel Operator is based:

$$grad(f) = \frac{\partial f}{\partial x} + \frac{\partial f}{\partial y}. \quad (2.22)$$

The Sobel Operator is known as a gradient filter because it replaces the original image with an estimate of the gradient of the image. See Figure 2.7 for two examples of Sobel edge-enhanced images.

The gradient provides an indication of the location and intensity or sharpness of the edges, or discontinuities, in an image, which usually impart the only useful information in an image to the observer. The Sobel Operator produces low output for uniform image regions (i.e. low spatial frequencies), and is also somewhat insensitive to noise effects (i.e. random high frequency content) [4]. Also, the HVS itself provides a form of edge detection [6]. This implies that the Sobel Operator acts as a type of spatial HVS filter. This research will investigate whether or not the variance

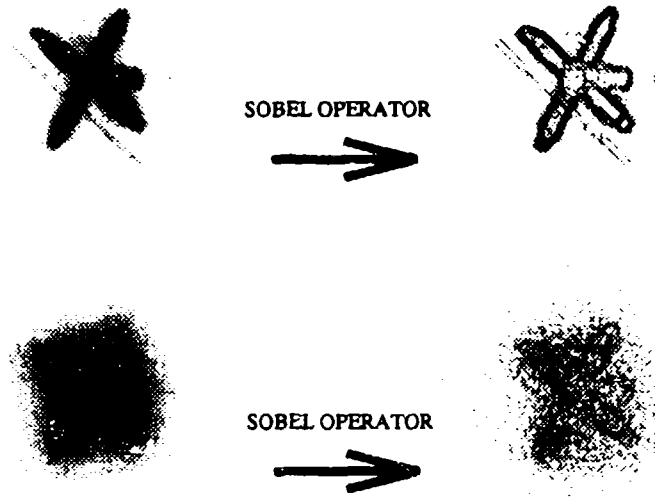


Figure 2.7 Sobel Operator Examples - Left: Original Images - Right: Sobel Filtered Images

image quality metric presented above will perform better if the image is first Sobel filtered.

Note that this idea has some support in the literature. One of the proposed sharpness functions proposed in [2] is the second moment of a partial derivative of the image, or:

$$\int dx dy \left| \frac{\partial^{m+n} f(x,y)}{\partial x^m \partial y^n} \right|^2 \quad (2.23)$$

where $f(x,y)$ is the image. This formulation is another approach to finding the variance of the edge information of an image. Another source [7] suggests analyzing the histogram shape of a Sobel-filtered image as a method of automatically detecting flaws in abrasive diamond film as it is being fabricated.

2.3 Summary

The following IQMs are to be tested, with results presented in Chapter 4:

1. Spectral Content (Band Limited) of Image

2. Variance of Original Image
3. Variance of Sobel Filtered Image

III. Research Approach

This chapter will discuss the methods used to test the various image quality metric candidates.

3.1 Adaptive Optics Simulation Software

Michael Roggemann of the Air Force Institute of Technology has developed FORTRAN software which simulates a general adaptive optics imaging system [16]. The user provides a "true" image as input to the system, say a CAD drawing of a satellite, such as the Russian Okean satellite model shown in Figure 3.2, and defines the simulation imaging parameters. The parameters, and some typical values used in this research are shown below:

SIMULATION PARAMETERS:	
number of frames	100
density of WFS detectors	10 across diameter
telescope mirror diameter	1.0 meters
wavelength of light	500 nanometers
target distance	500 kilometers
average number of photons per image	varied, 4th to 8th magnitude
average number of photons per WFS subaperture	varied, 4th to 8th magnitude
actuator spacing	11 centimeters
atmosphere coherence diameter, r_o	varied, 7 to 13 cm
RMS detector read noise	15 photons per pixel

The astronomical magnitude scale mentioned above is defined such that if the total radiation flux between two stars is given by the ratio s_1/s_2 , their magnitudes differ by $m_1 - m_2 = -2.512 \log_{10}(s_1/s_2)$, with a previously agreed upon flux level for $m = 0$. For example, the star Vega has an apparent magnitude of 0.14. If two objects

differ in absolute magnitude by 1, the number of photons leaving the objects differ by a factor of 2.512. If they differ by 5 magnitudes, the number of photons differs by a factor of 100. Roggemann [17] has numerically calculated the number of photons reaching an earth-bound adaptive optics telescope (through a typical atmosphere):

MAGNITUDE	No. Photons at Wavefront Sensor	No. Photons at Image Plane
4	207	10654
5	83	4262
6	33	1705
7	13	682
8	5	273

A block diagram of the major software simulator functions is shown in Figure 3.1.

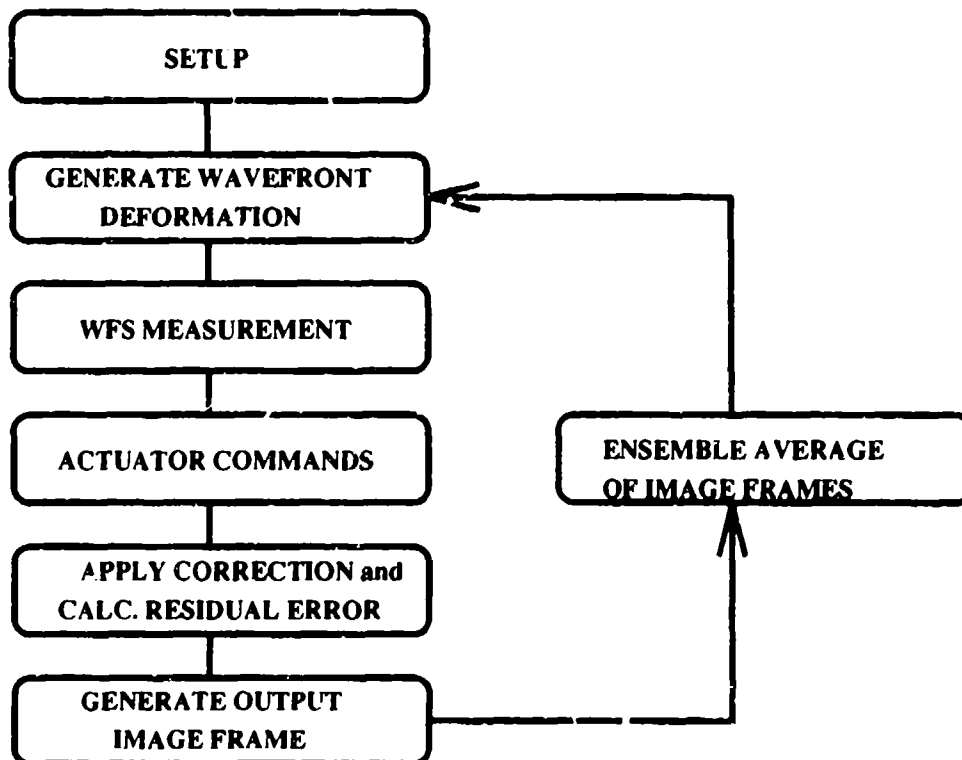


Figure 3.1 Block Diagram Description of Adaptive Optics Simulation Software

Two sets of output ensemble averages are shown below, first with magnitude held constant and τ_0 varying, then with τ_0 held constant and magnitude varying (Figures 3.3 and 3.4), and all other simulation parameters held constant throughout both cases. Note the different effects of the atmosphere and light level on resolution and quality.



Figure 3.2 Okean Satellite CAD Drawing



Figure 3.3 Okean Satellite, 4th magnitude, $\tau_0 = 13, 10,$ and 7 cm respectively

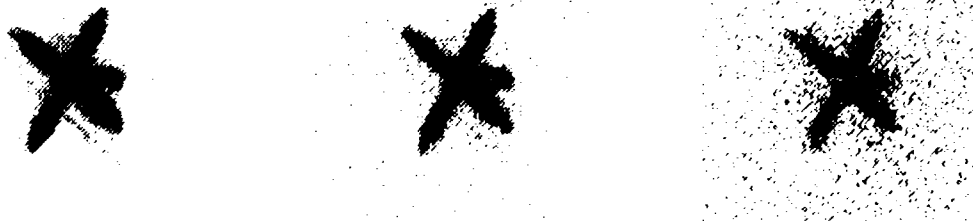


Figure 3.4 Okean Satellite, $\tau_0 = 13$ cm, 4th, 5th, and 6th magnitudes respectively

Besides the Okean satellite image, two other test objects were used in the simulation: (Figure 3.5) This variety of shapes, structures, and periodicities is assumed




Figure 3.5 Eorsat and Rorsat Imaging Target CAD Drawings

to provide a reasonable test of image quality measures as applied to space object imagery.

3.2 Testing Parameters

The optical propagation simulator gives the user direct control over three very important factors which have a direct bearing on AMOS image quality, but which cannot be known in advance in real-world operations:

1. Target Magnitude (light level);
2. Seeing Conditions (Fried Parameter); and
3. The original target irradiance function.

Since the goal is to detect differences in image quality, the actual values of the other parameters are somewhat unimportant, provided they are held constant while light level and seeing conditions are varied. For testing of raw imagery, the most straightforward procedure is to generate a large number of images for all three targets, varying magnitude and r_0 , calculate the various IQMs for these images, and plot the IQM values against both magnitude and r_0 .

As noted above, r_0 is a direct indication of image resolution. Therefore, a valid IQM should increase monotonically as a function of r_0 . Also, object magnitude impacts image quality through its effect on the performance of the adaptive optics

system (WFS measurement errors), and through its effect the image signal-to-noise ratio. A valid IQM should decrease monotonically as a function of magnitude.

One other test parameter will be considered in this research. When dealing with image coding, compression and transmission, *fidelity parameters* are commonly used, which provide a measure of how closely some "original" image, $f_{orig}(x, y)$ matches a "final" image $f(x, y)$ after undergoing some process. One common fidelity measure is *root-mean-square error*:

$$e_{rms} = \frac{1}{n^2} \sum_x \sum_y f_{orig}(x, y) - f(x, y) \text{ gray levels.} \quad (3.1)$$

It is well known that such fidelity measures are not good indicators of image quality as evaluated by the HVS. In other words, the HVS is known to be more tolerant of certain types of errors, and more sensitive to others [4]. For instance, in Figures 3.3 and 3.4 two different types of image corruption effects are noticeable, depending on the parameter being varied, yet e_{rms} would provide no information on which type was more or less objectionable to a human observer. However in both cases, e_{rms} would still increase with decreasing image quality. Therefore it may be instructive to parameterize IQMs against e_{rms} , to provide a coarse validity check of the results. It would be expected that valid IQMs should be a *generally* decreasing function of e_{rms} .

IQM performance on reconstructed (inverse filtered) imagery can also be parameterized against the triangular noise filter width. However, this filter width does not have a simple, easily quantifiable effect on image quality. If the filter is too narrow, the reconstructed image will be a low quality, low resolution "blob". If the noise filter is too wide, noise effects will lower the image quality. One possible test approach would be to reconstruct a single ensemble with a variety of filter widths, calculate IQMs for these various output images, and plot IQM versus noise filter width. One would expect a convex curve with maximum corresponding to the opti-

mum filter width. It would fall to the observer to determine subjectively if this filter width is indeed optimum.

The results of this testing are discussed in Chapter 4.

IV. Results

4.1 Introduction

This chapter investigates the hypothesis that the Image Quality Metrics (IQMs) presented in Chapter 2 correlate with atmospheric seeing conditions (r_o), target magnitude, and image fidelity (root-mean-square error), as controlled by the adaptive optics simulator discussed in Chapter 3. A key assumption is that these parameters are indeed indicative of Image Quality as experienced by AMOS operators and customers using real-world data. Key illustrative results are shown here, with the remainder in the appendix. This chapter also examines the idea of using the IQMs for reconstructed image selection, specifically, selection of a reconstruction noise filter.

In all cases a successful IQM will consistently and monotonically change with a quantifiable change in r_o or target magnitude, as controlled by the image simulator. The two dimensional surface plots shown in the following two sections of this chapter will plot r_o on one axis, target magnitude on the second axis, and the IQMs as a function of the two. The IQMs should give the high-resolution, high brightness images represented by one corner of the plot domain the highest quality rating and the low-resolution, low brightness images represented by the opposite corner of the plot domain the lowest quality rating. Similarly, any cross section taken parallel to the r_o or magnitude axes should give a monotonically increasing quality rating curve as either r_o goes up or magnitude goes down.

Metrics were also parameterized against RMS error. Recall from Chapter 3 that RMS error only correlates approximately with image quality as perceived by the human visual system. However, observing the relation between IQMs and RMS error should prove to be an instructive, qualitative, overall check on the validity of the other results.

4.2 Spectral Image Quality Metrics

Recall from Chapter 2 that the band limits for the spectral metric are best determined empirically. This is because the display, image frame size, and the spatial bandwidth of the particular telescope system in use are all system dependent and all effect the image spectra as sampled by the FFT algorithm. Figure 4.1 shows an example of how this was accomplished for the simulated imagery used in this research. A simple, practical approach for band limit selection is adopted here: since the goal is discrimination between images based on quality, observe where the radially averaged spectra of different quality images intersect. As mentioned in Chapter 2, the area under the curve segments between these two intersection points is sensitive to image quality, so these two intersection points are a practical indication of the HVS passband. This passband can be determined by inspection.

The radially averaged magnitude spectra (normalized to unit area) are shown for 5 images of the Okean satellite (Figure 4.1). In this case, the Fried Parameter was held constant, and the target magnitude was varied. Note that for this image format, for radial frequency distances of about 1 to 15 samples of normalized frequency, the curves corresponding to any particular image are greater than the curves corresponding to a lower quality image. A similar effect is found for the second plot, where the magnitude was held constant and the Fried Parameter was varied (Figure 4.2). Determining the frequencies at which the radially averaged magnitude spectra of different quality images overlap seems to be a reasonable functional method of determining the HVS passband. For this particular image format and (simulated) telescope system, the band limit was therefore chosen to go from 3 to 11 pixels radial frequency distance. This type of empirical determination would have to be accomplished by inspection for any different image format or telescope system. The IQM algorithm merely adds up the magnitude spectrum pixels falling within this distance range from the zero frequency origin.

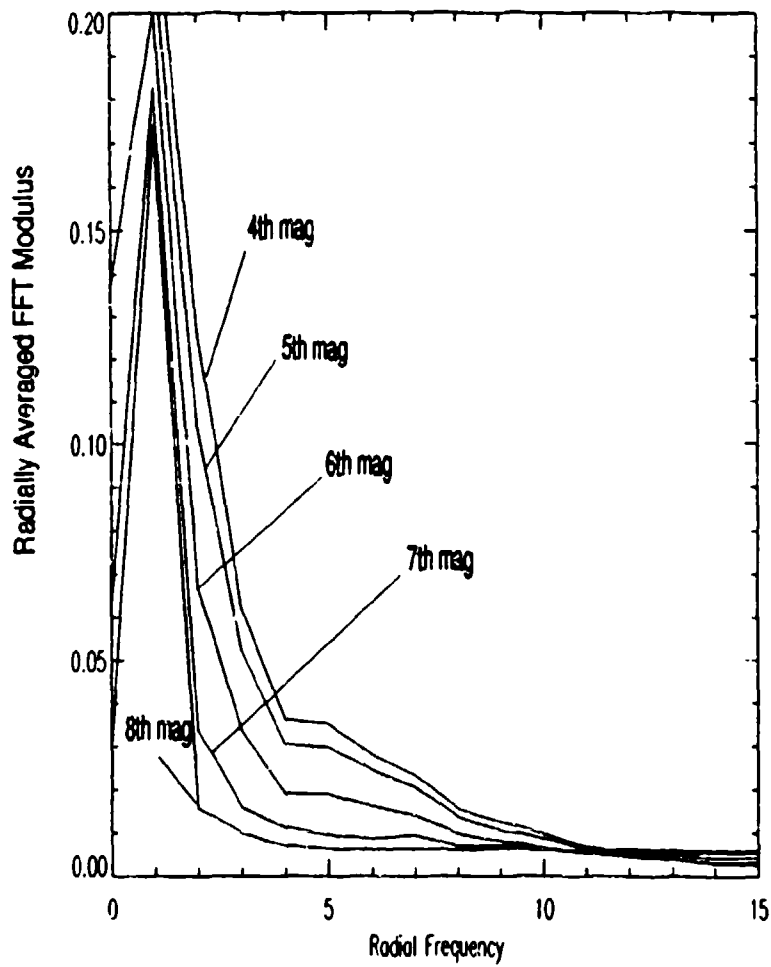


Figure 4.1 Radially Averaged Magnitude Spectra, $\tau_o = 10$ cm, 5 Different Magnitudes, Okean Satellite Image

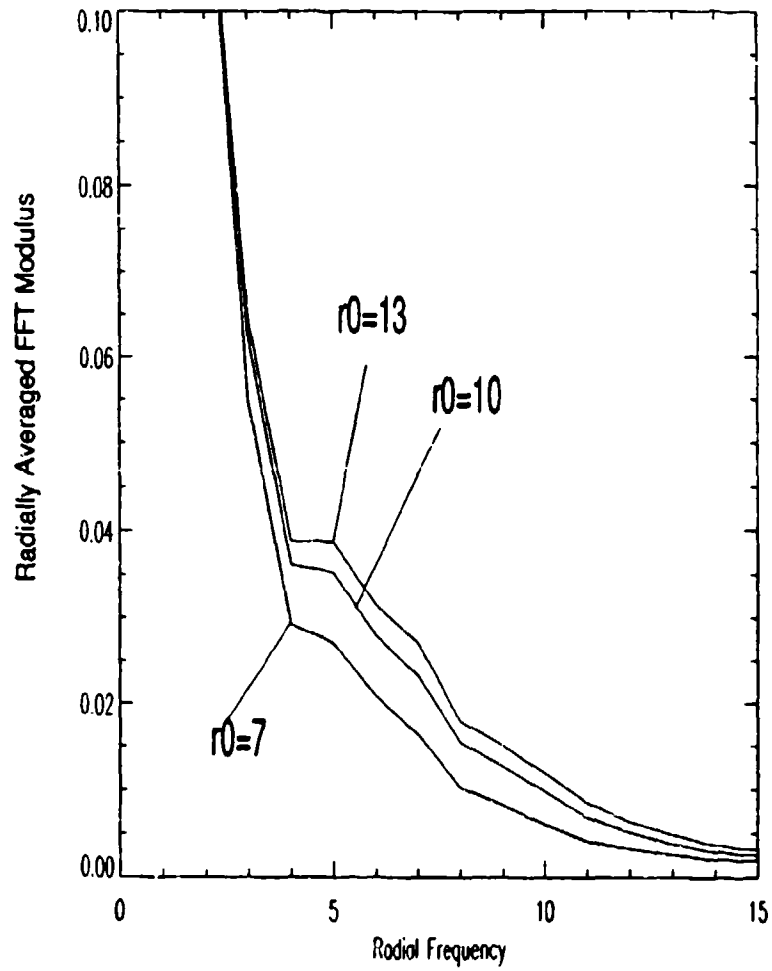


Figure 4.2 Radially Averaged Magnitude Spectra, 4th Magnitude, 3 Different r_0 's, Okean Satellite Image

A representative surface plot from the Okean target spectral IQM experiment is shown in Figure 4.3. Cross-sections of this surface plot are shown in Figures

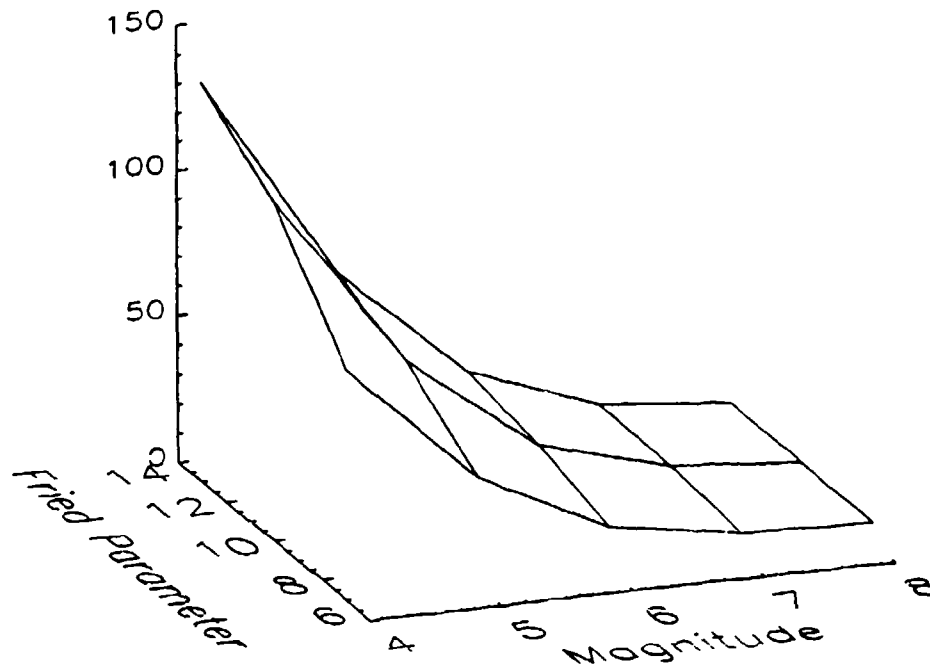


Figure 4.3 Spectral IQM Parameterization, Okean Satellite Image

4.4 and 4.5.

This IQM gives similar results for the other two test objects, as shown in the appendix. The metric is monotonically increasing with r_o and with brightness (decreasing with magnitude). This appears to be a successful Image Quality Metric.

As a validity check, the Quality metric is plotted vs. RMS error. Note the approximate trend of decreasing quality rating with increasing RMS error. This lends weight to the hypothesis that this is a valid quality metric. Recall, as mentioned previously, that fidelity metrics like RMS error correlate only approximately with HVS-perceived image quality.

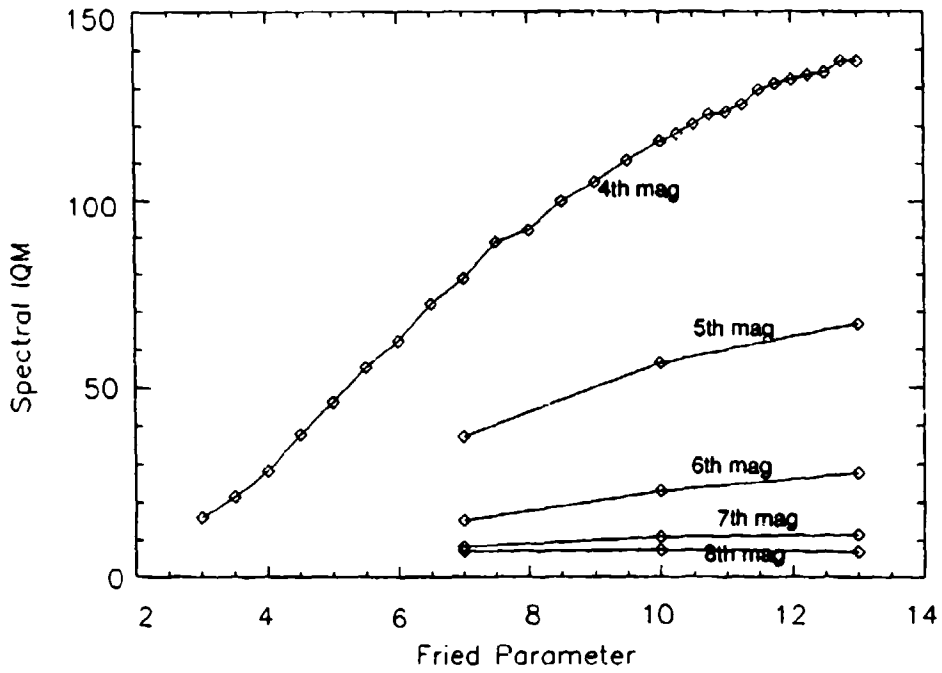


Figure 4.4 Spectral IQM vs Fried Parameter, Okean Satellite Image

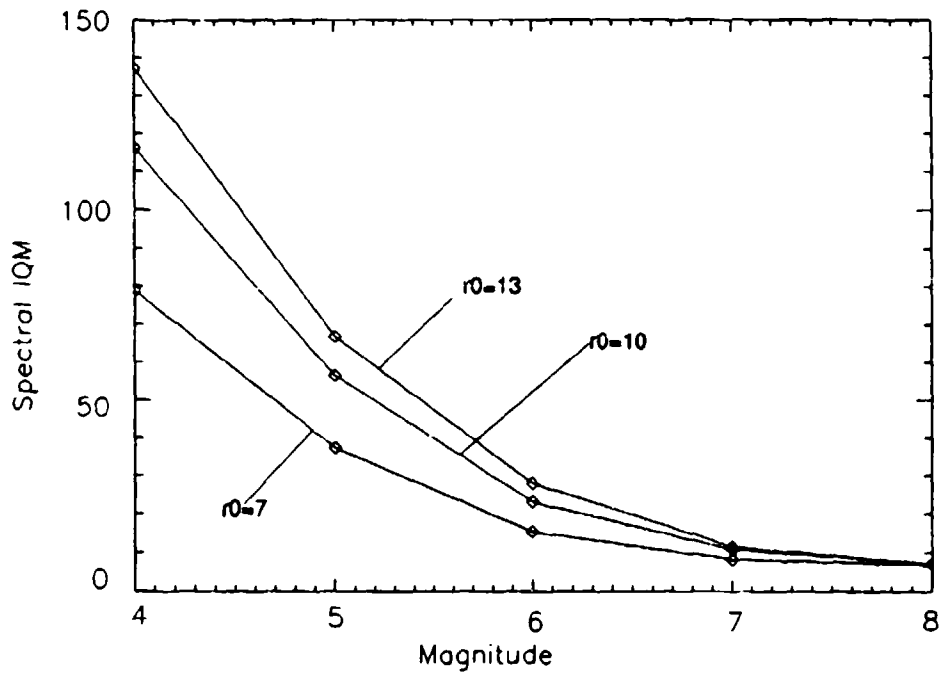


Figure 4.5 Spectral IQM vs Target Magnitude, Okean Satellite Image

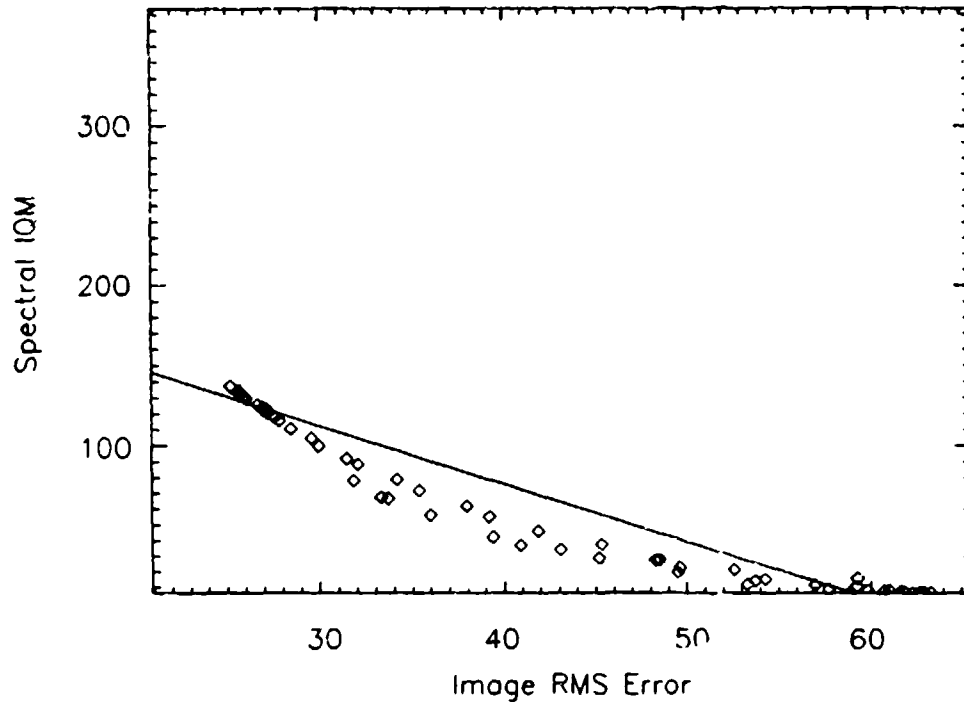


Figure 4.6 Spectral IQM vs RMS Error, Okean Satellite Image

4.3 Histogram-Based Image Quality Metrics

A representative surface plot from the Okean target Variance IQM experiment is shown in Figure 4.7. Cross-sections of this surface plot are shown in Figures 4.4 and 4.5.

The metric performs reasonably well for brighter objects, but as the objects get dimmer that 6th magnitude, the performance curve slope changes sign. Observe Figure 4.10, which shows the Okean satellite with $r_o = 7cm$ and magnitudes of 6,7, and 8 respectively. Judging from the curve in Figures 4.7 , 4.8 and 4.9, the two lower quality images have “spoofed” the variance metric into categorizing them as better than the higher quality 6th magnitude image (Figure 4.7). As discussed in Chapter 2, pixel position information is not captured by the histogram moments. The 7th and 8th magnitude images shown do indeed have more “variance” than the 6th magnitude image, but this increased variance is not due any higher detail

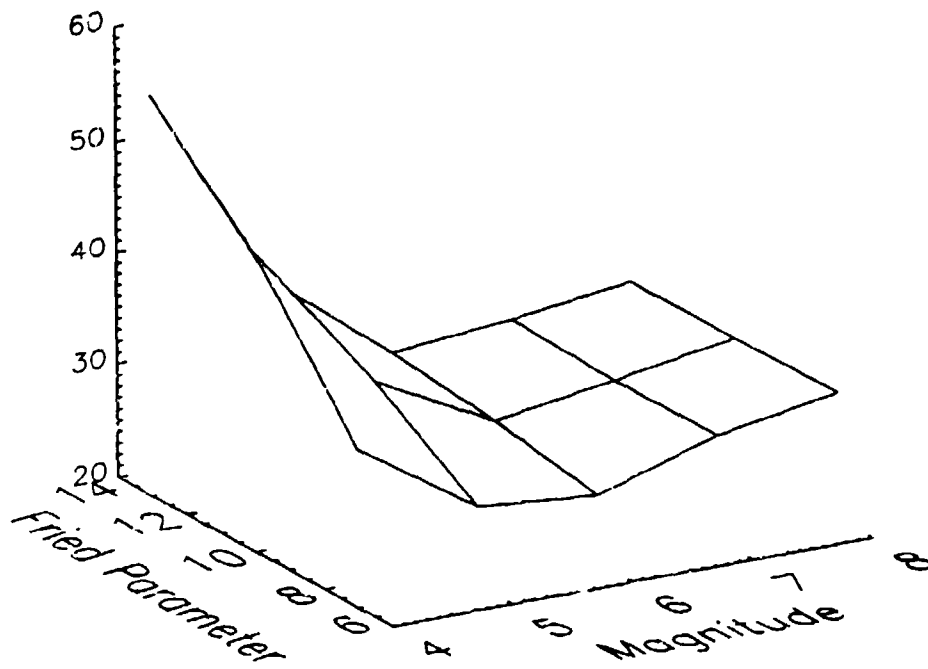


Figure 4.7 Variance IQM Parameterization, Okean Satellite Image

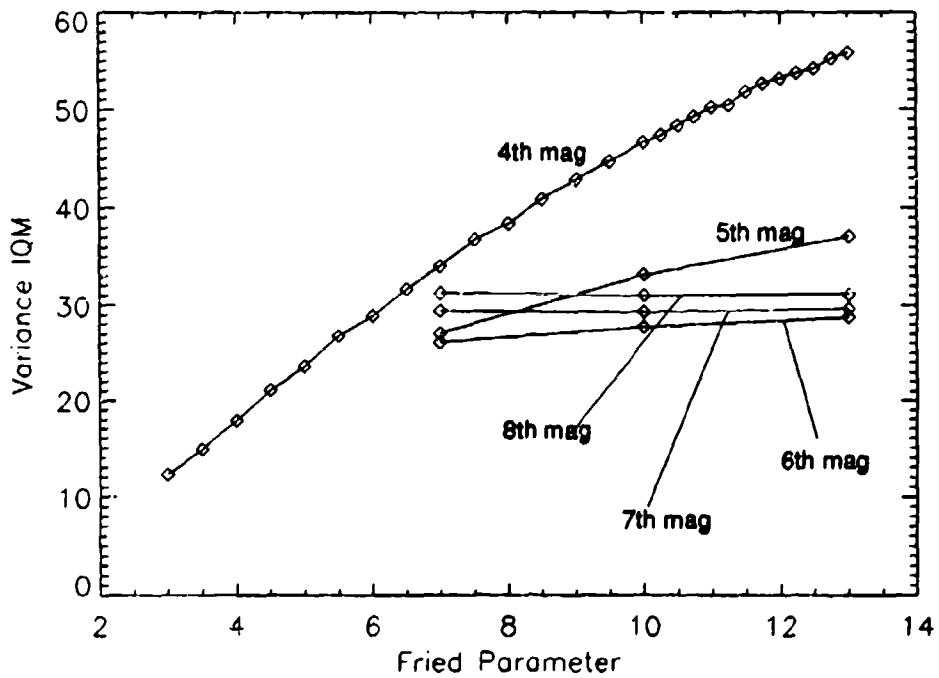


Figure 4.8 Variance IQM vs Fried Parameter, Okean Satellite Image

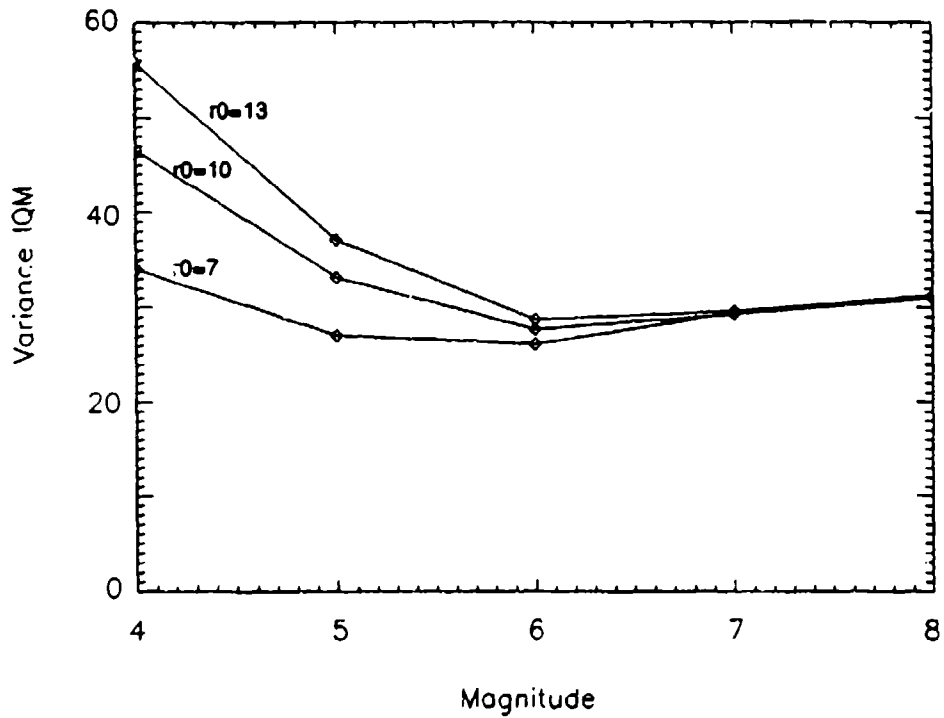


Figure 4.9 Variance IQM vs. Target Magnitude, Okean Satellite Image

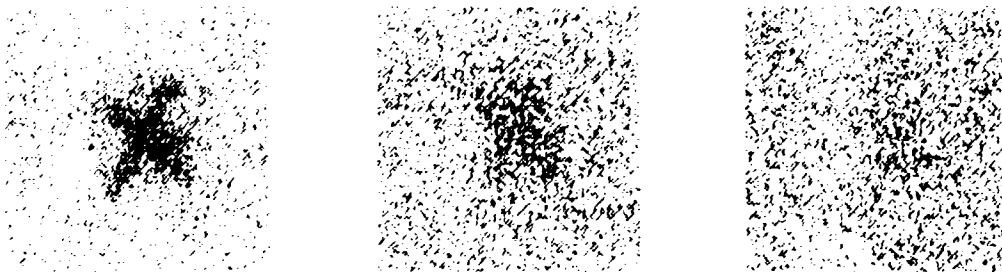


Figure 4.10 Okean Satellite, $r_o = 7cm$ and magnitudes of 6,7, and 8 Respectively

or meaningful structural content of these images. It is instead due to the lower signal-to-noise ratio of the dimmer images.

Observe how the two lower quality images in question have little in the way of edges or discontinuities. It seems reasonable that if a Sobel operator were applied to these images and then the variance were calculated, relative variance-based quality rating of these images would be reduced, since there is less energy content in these images that would survive the Sobel operation. A parameter plot of the Sobel-Variance IQM is shown in Figures 4.11, 4.12 and 4.13, verifying this hypothesis.

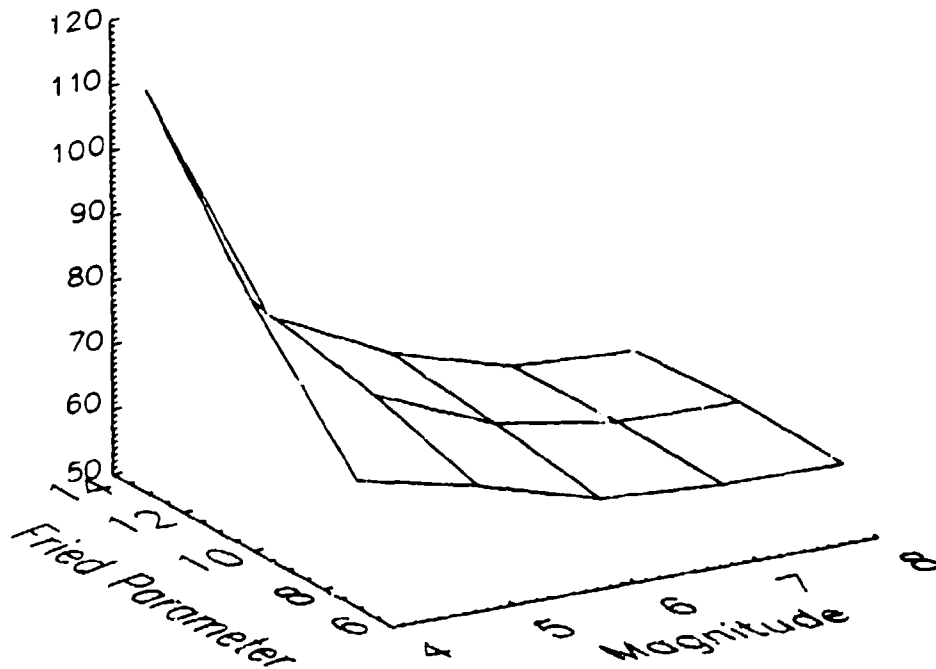


Figure 4.11 Sobel-Variance IQM Parameterization, Okean Satellite Image

AMOS users could determine whether the Sobel extension of the variance metric is necessary. If the signal-to-noise ratio rarely drops low enough to spoof the variance IQM, the Sobel operation may be unnecessary. However, it costs little in the way of computation time, and the algorithm exists in "canned" form in the IDL software package.

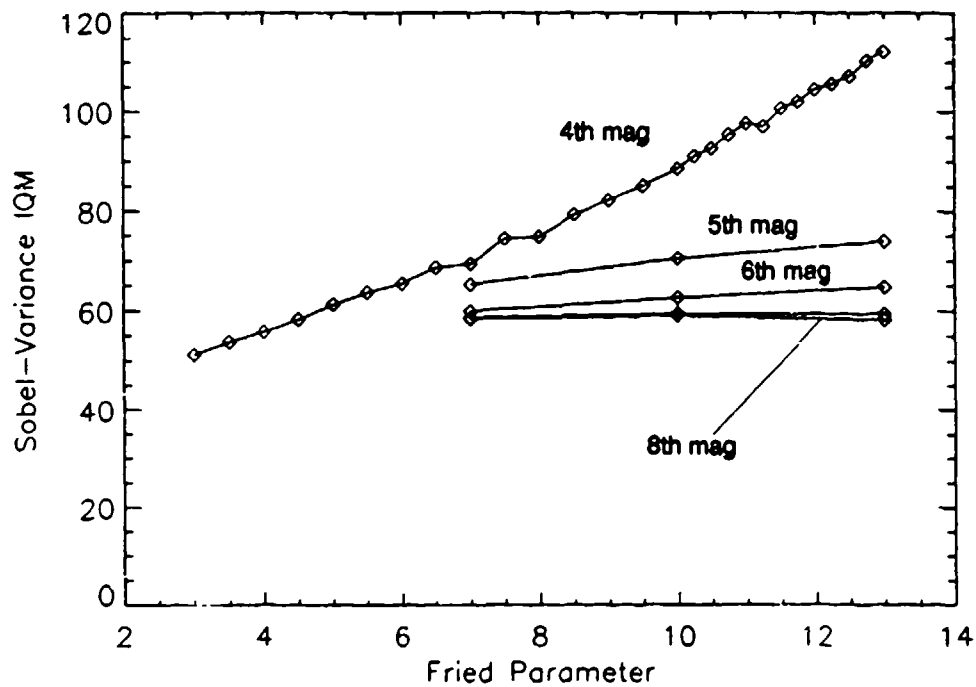


Figure 4.12 Sobel-Variance IQM vs Fried Parameter, Okean Satellite Image

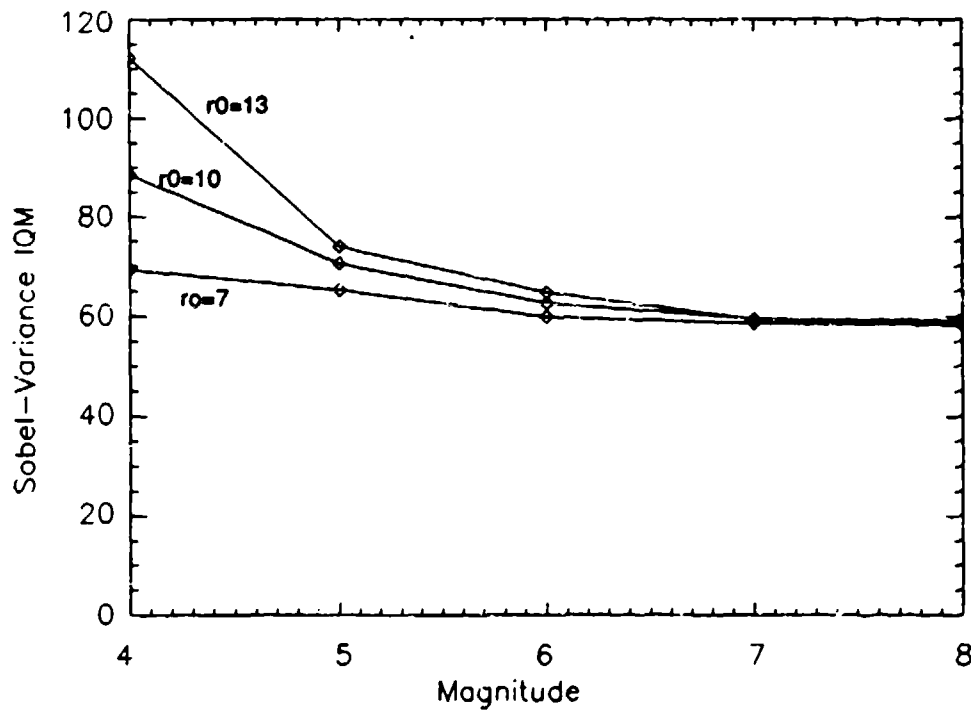


Figure 4.13 Sobel-Variance IQM vs Target Magnitude, Okean Satellite Image

Although there are now indications that variance alone is not a consistent indicator of image quality, it is instructive to include it in discussions which follow, for comparison with the Spectral and Sobel-Variance IQMs.

The RMS parameter plots for the regular and Sobel variance IQMs are shown in Figures 4.14 and 4.15. An interesting feature of these plots is the two "arms" that

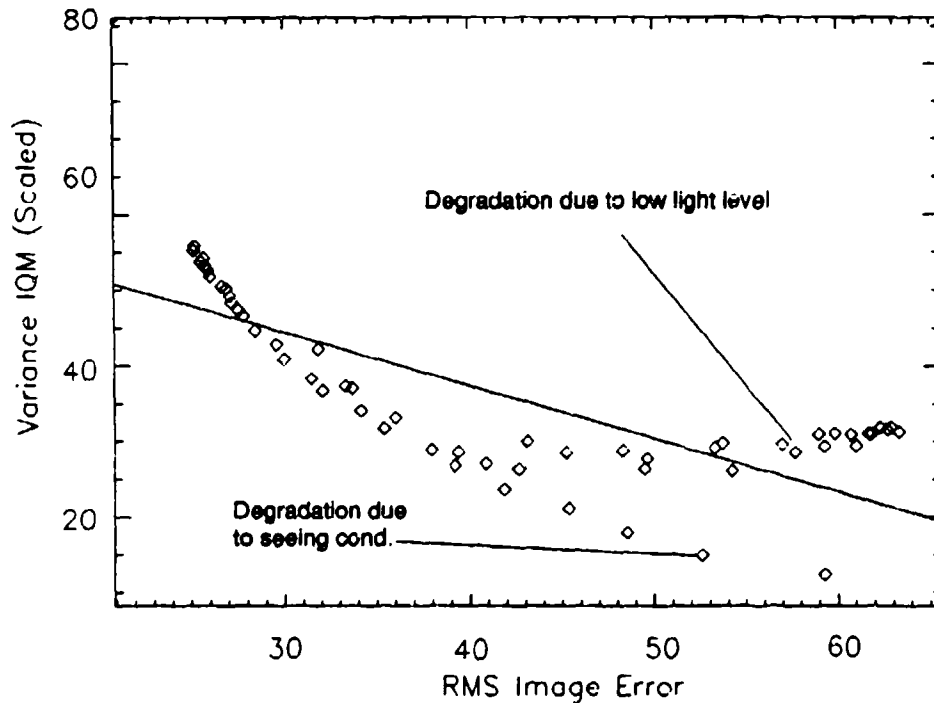


Figure 4.14 Variance IQM vs. RMS error, Okean Satellite Image

split off from the curve at high RMS error levels. The upper arm corresponds to the low signal-to-noise ratio as the images get dimmer and dimmer. The lower arm of the plot corresponds to the image blurring as r_s gets smaller and smaller. Notice that if the degradation were only related to seeing conditions, the Sobel extension to this metric would not be necessary. The implication is that degraded seeing conditions do not increase variance.

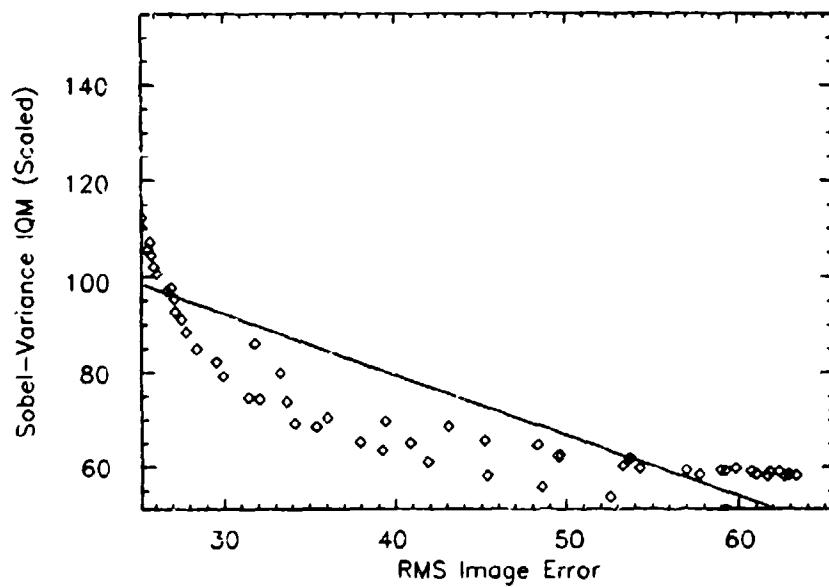


Figure 4.15 Sobel-Variance IQM vs. RMS error, Okean Satellite Image

The final histogram based metric discussed was entropy. This metric would be expected to give a lower number as image quality increased [2] [1]. This turned out to be the case when only seeing condition were varied (Figure 4.16).

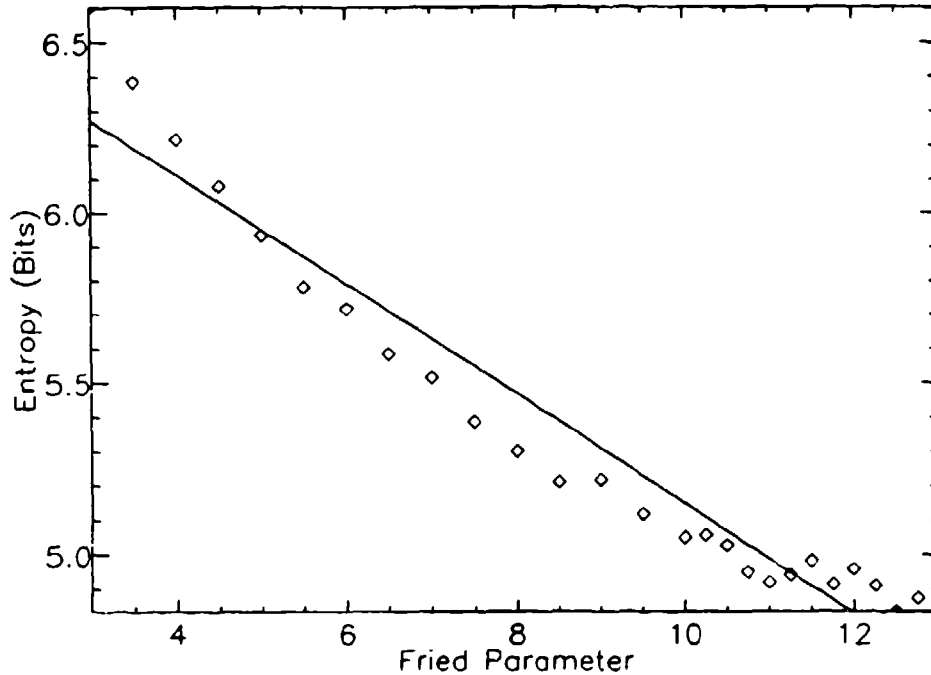


Figure 4.16 Entropy vs. τ_o (cm), Okean Satellite Image

However the entropy metric responded in the opposite manner as the magnitude of the image increased (became dimmer). Figure 4.17 shows this for $\tau_o = 10$ and 13 cm.

The conclusion is that entropy is not a consistent metric, since it gives higher quality ratings for lower SNR images. Since image degradations caused by low magnitude (low SNR) do not occur separately from degradations caused by seeing conditions, this metric is operationally unacceptable. Although entropy is functionally related to histogram shape, this relationship is apparently not reliable in terms of passing image quality information. Preliminary investigations into measuring the entropy of edge-enhanced images also showed the same inconsistency as above, showing higher quality for lower SNR.

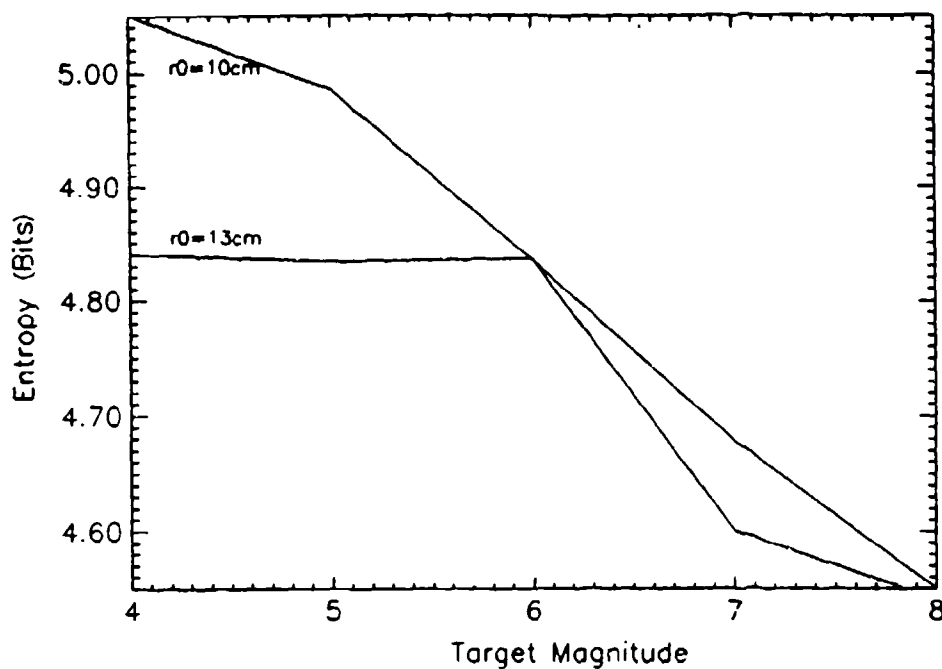


Figure 4.17 Entropy vs. Magnitude, Okean Satellite Image

Although all unsuccessful metrics are not presented in this thesis, entropy is an important theoretical concept throughout a wide variety of engineering disciplines. It is also a logical candidate to consider for quality measurement, since it intuitively relates to “information content” of signals, which is itself one possible definition of “quality”. For this reason, it merits special mention.

4.4 Reconstructed Image Selection

From an observing session of a low earth orbit space object, AMOS customers usually require two images as the object climbs from ascending horizon to zenith, one image captured as the object is approximately near zenith, and two more as the object ascends to the other horizon. This means dozens of 50 to 100 exposure ensembles (each of which is reconstructed to form a single output image) to choose from.

Furthermore, each image reconstruction via inverse filtering is reconstructed with a number of triangular noise filter widths. As noted in Chapter 1, since the OTF of the telescope system is a random variable through time, the optimum width of this filter is best determined empirically. This means reconstructing the image with a number of filter widths and subjectively selecting the best product. This last aspect of image product selection is investigated here. Any conclusions drawn could also be applied to the selection problem mentioned in the previous paragraph.

It is expected that very narrow filter widths would result in output images that were low-resolution, low-quality "blobs", since the high frequency detail would be filtered away. Very wide filter widths, on the other hand, could be expected to allow in high frequency noise content, also lowering image quality. Therefore, some intermediate filter width would be desired. The hypothesis to be examined here is that plotting an IQM as a function of noise filter width would produce a convex curve, with the maximum of the curve corresponding to the optimum filter width.

First consider the reconstructed satellite images shown in Figure 4.18. The source ensemble is 100 exposures of the Okean target, with an r_o of 5 centimeters and practically infinite (one million photons per frame) brightness. This means high signal-to-noise-ratio. The IQM values in this experiment for the Spectral, Variance, and Sobel Variance IQMs are shown in Figure 4.19. In this experiment, the Spectral IQM rates the third image, with filter radius 12, as the best. The Sobel-Variance IQM rates the fourth image, with filter radius 16 as the best. The Variance IQM rates the 6th image, with filter radius 20, as the best.

The next experiment is with the same target, but with $r_o = 10$ centimeters, and a target magnitude of 6 (Figure 4.20). The IQM values in this experiment for the Spectral, Variance, and Sobel Variance IQMs are shown in Figure 4.21. Again, the peaks of each of the three curves can be picked off the graph. The Spectral IQM picked the third image, with noise filter radius of 12, as the best image. The Sobel-Variance Metric picked the second image, with noise filter radius of 8, as the

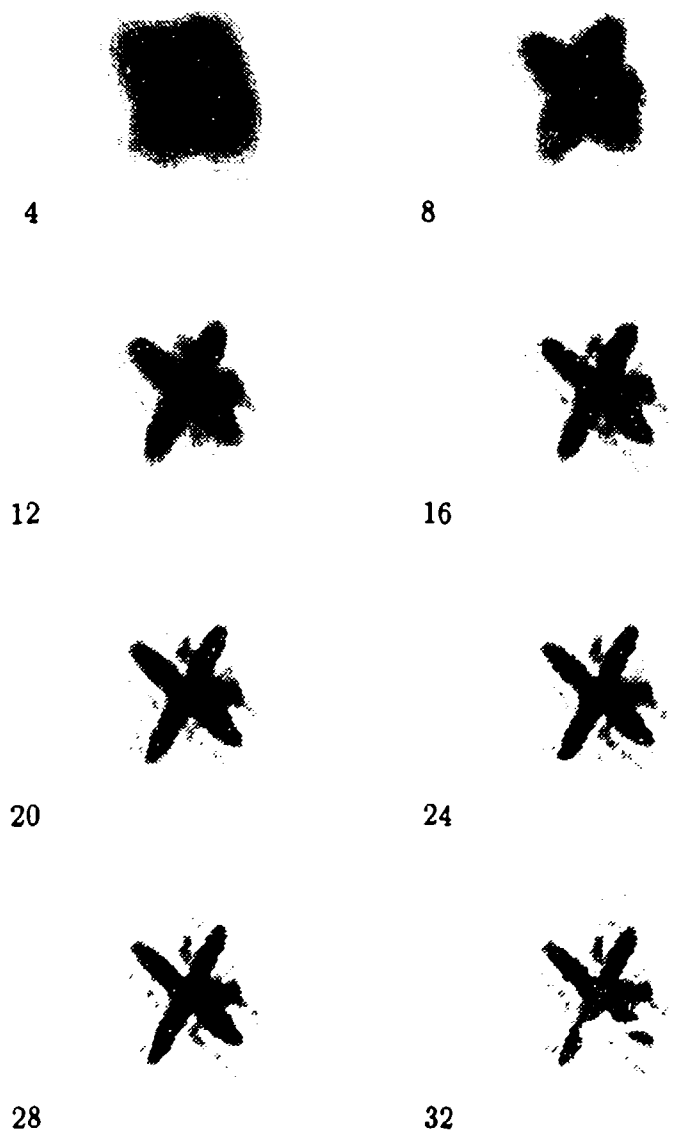


Figure 4.18 Okean Target Reconstructed Images, High SNR, $r_o = 5\text{cm}$, Noise Filter Base Radii = 4,8,12,16,20,24,28, and 32 Pixels Respectively, From Left to Right, Top to Bottom

IQM Response as a Function of Reconstruction Noise Filter Width

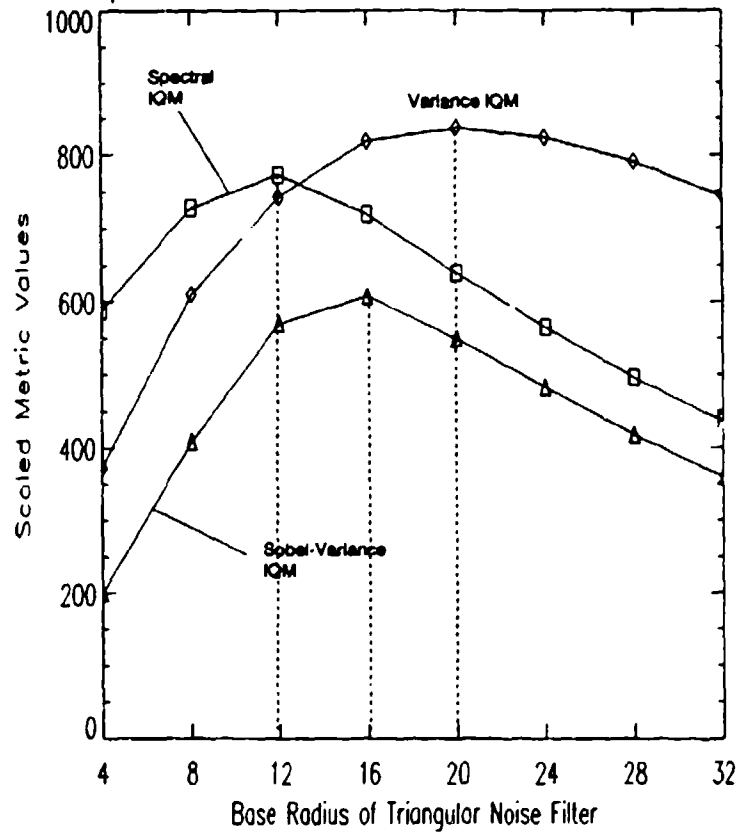


Figure 4.19 IQM Selection of Noise Filter Radius, Okean Target Reconstructed Images, High SNR, $r_o = 5\text{cm}$

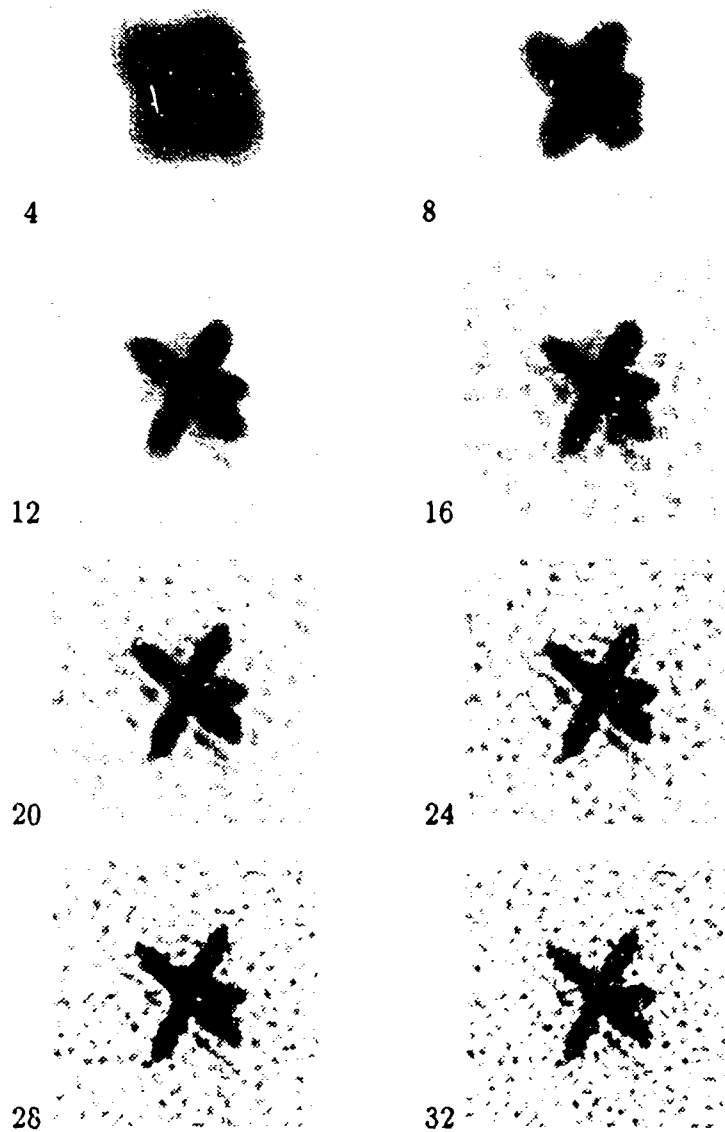


Figure 4.20 Okean Target Reconstructed Images, 6th magnitude, $\tau_o = 10\text{cm}$, Noise Filter Base Radii = 4,8,12,16,20,24,28, and 32 Pixels Respectively, From Left to Right, Top to Bottom

IQM Response as a Function of Reconstruction Noise Filter Width

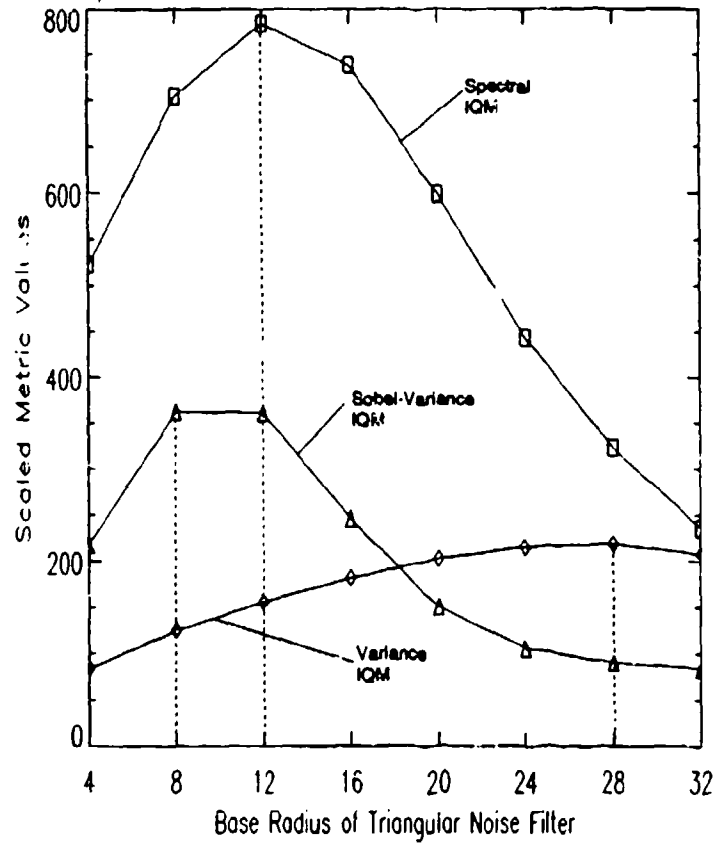


Figure 4.21 IQM Selection of Noise Filter Radii, Okean Target Reconstructed Images, 6th magnitude, $\tau_o = 10\text{cm}$

best image. Notice this time that the Variance IQM gives a result significantly different from the other two IQMs, selecting the image with noise filter radius of 28. This is because noise effects have been introduced into the experiment, due to the low target magnitude. As mentioned earlier in this chapter, the Variance IQM is "spoofed" by high levels of noise in the image. This may be an explanation of the result shown in Figure 4.21, where the Variance IQM is selecting reconstructed images with significantly higher noise levels than the other two IQMs. Notice also, that even though r_o has increased from its value in the first experiment, which would effectively increase the bandwidth of the image, the optimal filter radius for the Spectral and Sobel-Variance metrics decreased, because of the need to keep out the noise that was not present in the first experiment.

The third and final experiment presented in this section is a 5th magnitude Eorsat target, with $r_o = 7$ centimeters. The reconstructed images are shown in Figure 4.22, and the IQM results are shown in Figure 4.23..

Notice in Figures 4.20 and 4.21, for example, when significant noise is present, that the variance metric is again fooled by noise. In all the cases shown above, Spectral and Sobel Variance IQMs react quite similarly, and appear to not be spoofed by noise artifacts. Surface plots parameterizing these two IQMs (Spectral and Sobel-Variance) against r_o and noise filter width are shown below. Notice that these plots show that when magnitude (and signal-to-noise-ratio) is changed, optimum filter width is changed. Optimal filter width also changes when r_o (and the effective telescope bandwidth) is changed.

Notice that the performance of the metrics compared to r_o and magnitude on *reconstructed* images is similar to the performance on "raw" ensembles, so these metrics are equally valid for comparing either raw or reconstructed imagery, assuming in reconstructed image case that comparisons are only between images that used triangular noise filters of the same width. This conclusion can be drawn immedi-

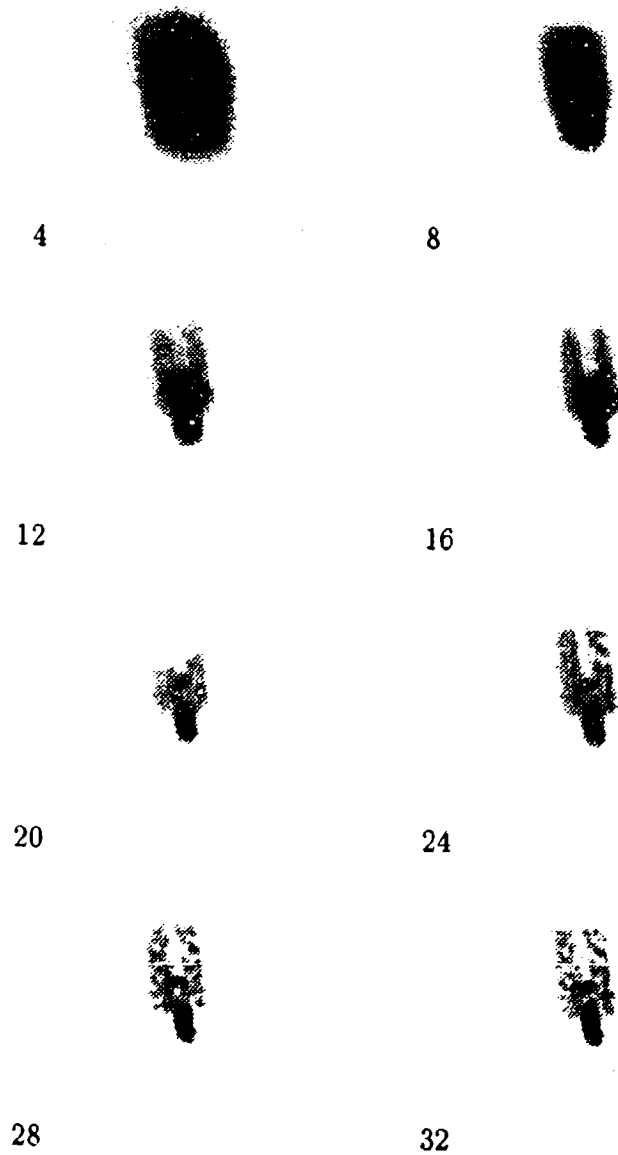


Figure 4.22 Eorsat Target Reconstructed Images, 5th magnitude, $r_o = 7\text{cm}$, Noise Filter Base Radii = 4,8,12,16,20,24,28, and 32 Pixels Respectively, From Left to Right, Top to Bottom

IQM Response as a Function of Reconstruction Noise Filter Width

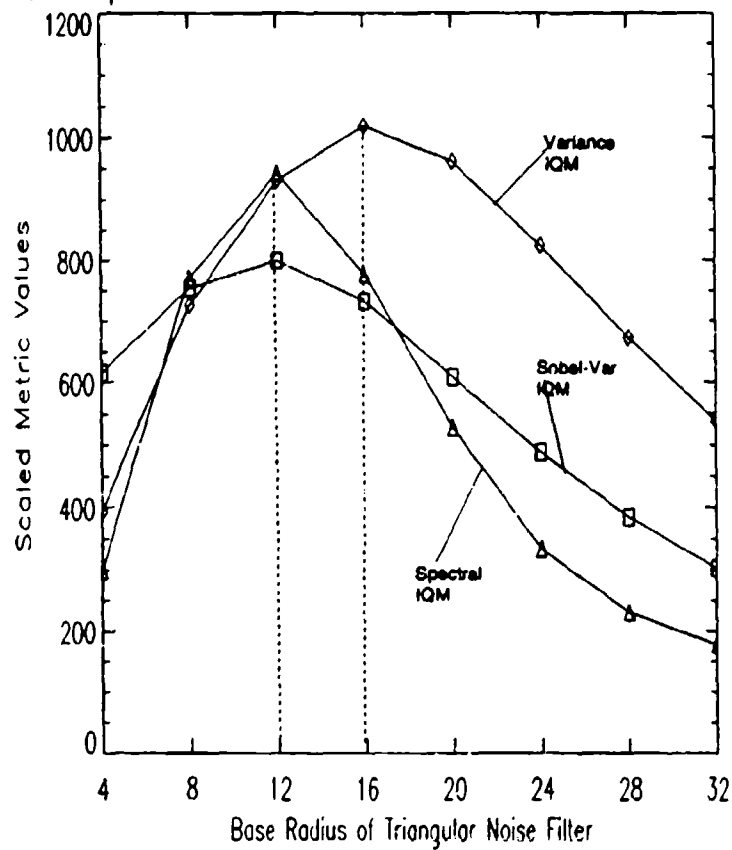


Figure 4.23 IQM Selection of Noise Filter Radius, Eorsat Target Reconstructed Images, 5th magnitude, $\tau_o = 7\text{cm}$

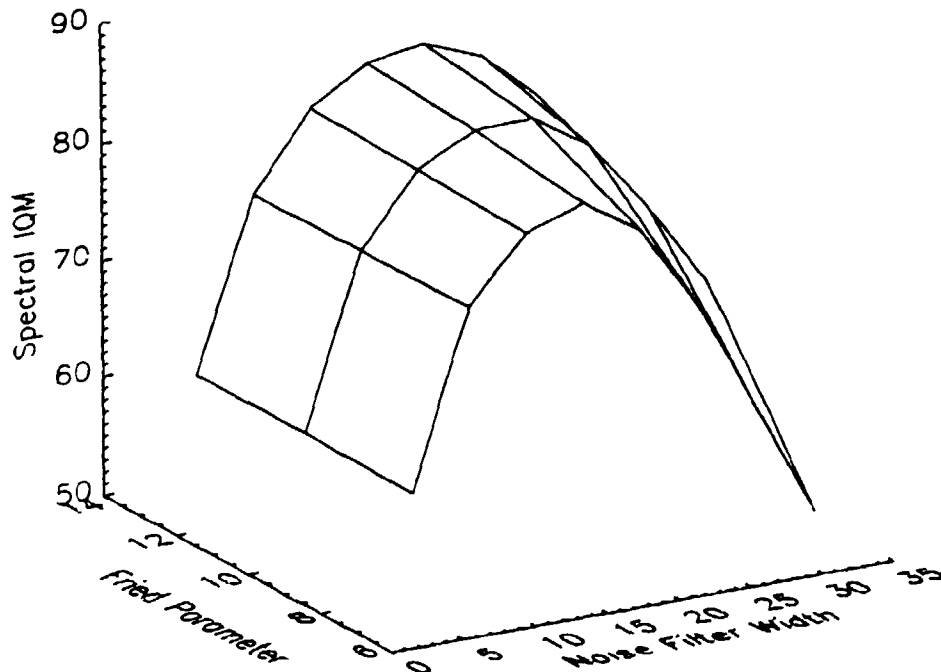


Figure 4.24 Spectral IQM vs. τ_o and Noise Filter Radius, Okean Satellite Image, Magnitude = 4

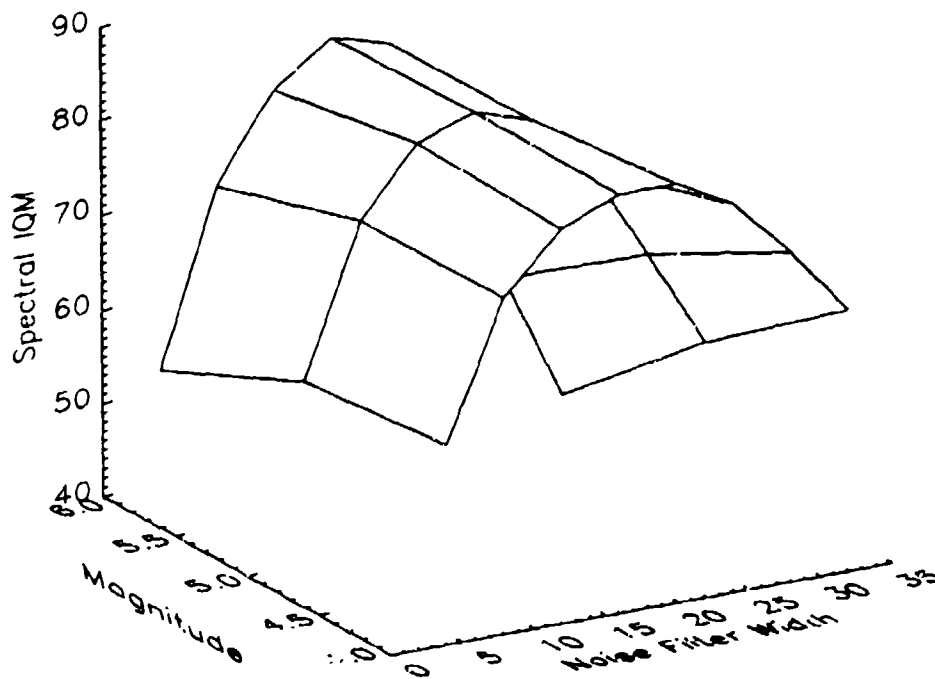


Figure 4.25 Spectral IQM vs. Target Magnitude and Noise Filter Radius, Okean Satellite Image, $\tau_o = 10$ cm

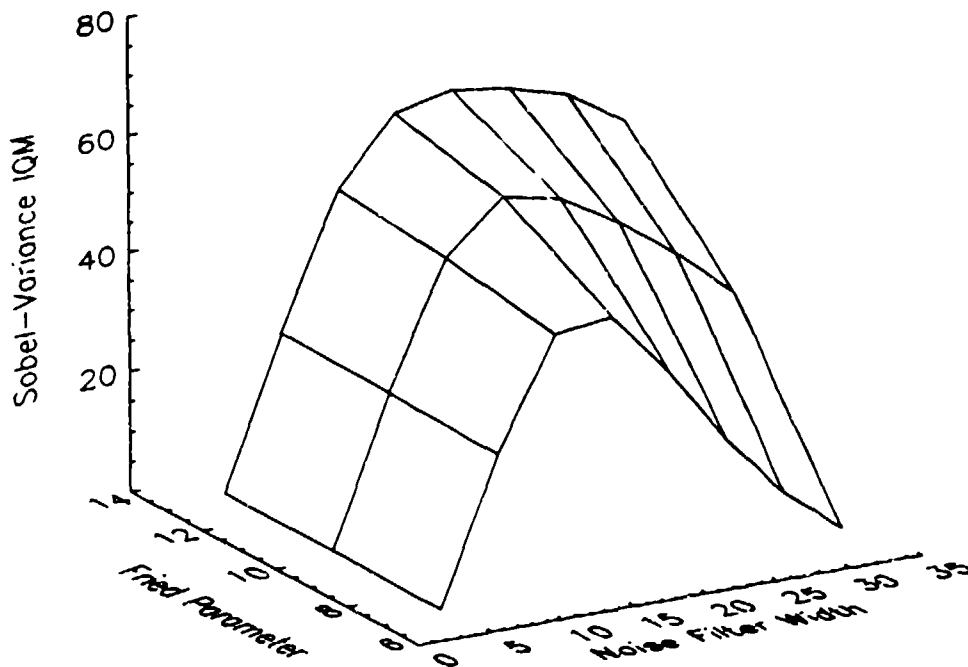


Figure 4.26 Sobel-Variance IQM vs. r_o and Noise Filter Radius, Okean Satellite Image, Magnitude = 4

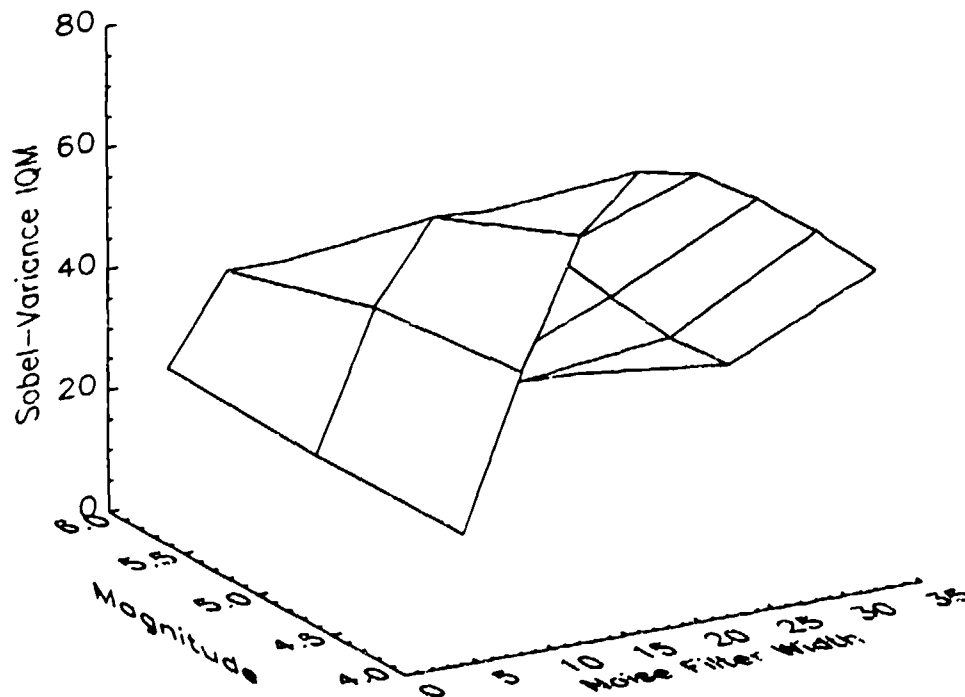


Figure 4.27 Sobel-Variance IQM vs. Target Magnitude and Noise Filter Radius, Okean Satellite Image, $r_o = 10$ cm

ately since it is agreed that r_o and magnitude are themselves immediate, monotonic indicators of image quality.

However when using the IQMs for reconstructed imagery with different noise filter widths, such as in the plots above, notice that different metrics select different filter widths as "best". The user of the IQM will have to decide which, if any of these metrics are to be used when comparing imagery of different noise filter widths.

4.5 Summary of Results

On all images tested, the Spectral and Sobel-Variance Image Quality Metrics give indications of being successful Image Quality Metrics for both raw and reconstructed images. The Spectral IQM cannot be implemented in a particular system until the appropriate band limits are empirically determined, as discussed above. The Sobel-Variance IQM requires no such analysis, and provides practically the same capability for un-supervised discrimination of images based on quality.

The Spectral and Sobel-Variance IQMs have been conceptually validated on a database of raw satellite imagery. A feasibility argument has also been presented for using these two IQMs to select optimum reconstruction noise filter bandwidth. The two IQMs can give slightly different results, in which case a subjective assessment is required to decide which IQM to use for this purpose.

V. Conclusions and Recommendations

5.1 Thesis Summary

This thesis project has dealt with the problem of "measuring" the quality of a digital image, specifically a digital image of an orbiting satellite, as observed from a ground-based, adaptive-optics telescope, through the Earth's atmosphere.

The challenge of this problem lies in the well-established fact that "image quality" is very much in the eye of the beholder. It is often taken for granted that the best assessment of image quality necessarily includes a subjective evaluation by the person who will be using the imagery. This is a very serious restriction if a quality assessment is required in an image processing application.

Consider, for example, the thesis sponsor, the Air Force Maui Optical Station, AMOS, which captures high resolution imagery of orbiting space objects. During a particular observing session, hundreds of raw image frames may be gathered for post processing. Some of these images are of lower quality than others, and it is assumed desirable to exclude them from post processing. In order to do this, the human operator must manually observe each of the raw image frames and subjectively decide which images to exclude. Similarly, when using post processing to digitally reconstruct the imagery, there are a variety of post-processing techniques available, and the techniques all include user defined variables to be adjusted based on trial-and-error and subjective judgement. The user must subjectively select the optimum reconstruction technique and parameters.

If there were a way for the computer to assign a "quality number" to the images, the above processes could conceivably be fully automated. The selections of best and worst images could be reduced to a simple thresholding the the quality number.

This thesis investigated a variety of quantities which a computer could automatically extract from a digital image, testing whether they correlate with image quality, as defined for AMOS imagery. The two most successful *image quality metrics* (IQMs) were

1. A *spectral IQM* which involved measuring the spectral (Fourier domain) content of the image within the passband of the human visual system; and
2. A *Sobel Variance IQM* which involved finding the sample variance of a Sobel-enhanced image.

It was shown that through Parseval's theorem these two metrics are conceptually related.

It is important to recall that metrics can only be meaningfully compared if

- all images are of the same object
- that object is at relatively the same orientation (i.e. from the same short time-span during an AMOS pass
- all images are normalized to the same total energy.

Also, the human visual system passband is most easily and practically determined by inspection as discussed in Chapters 2 and 4.

These metrics were tested against a database of satellite images which were created by an adaptive optics software simulation. This computer simulation allowed the user to quantitatively specify the two parameters which physically determine AMOS image quality: target brightness and atmospheric seeing conditions. A library of images for three typical space objects was created, while systematically varying these two simulation quality parameters. Any prospective IQM could then be tested against this image library. A successful IQM would be expected to give consistent, quantifiable changes in image quality ratings as these simulation parameters changed

value. The Spectral and Sobel-Variance IQMs gave consistent and reasonable results for this test database of images.

After the validity of the IQMs was tested on raw imagery, the problem of reconstructed image selection was examined. One of the most common image reconstruction techniques used at AMOS is a modified inverse filtering approach, requiring a user-specified noise attenuation filter. Some of the above library images were reconstructed with a variety of noise filter widths and then evaluated with the Spectral and Sobel-Variance IQMs. The results show that these IQMs might reasonably be used to automatically select the optimum reconstruction parameters. Since the two metrics sometimes gave different results, the user might best determine which of the two acquires the best track record on actual, operational imagery, in the course of adopting these concepts into a fully automated image reconstruction system.

5.2 Further Research

The inverse filtering reconstruction process can often cause noise "artifacts" to be introduced into the final image. Some sort of texture-based segmentation of these noisy reconstructed images, to remove these artifacts might increase the validity of the IQMs in reconstructed image selection. Using the IQMs themselves on small subregions of the image might even prove to be a good method of segmentation. Of course, with segmentation there is always the risk of accidentally eliminating valid image information.

It has also been suggested that instead of approximating the human visual system MTF as a simple rectangular bandpass, the more exact exponential formulation shown in Chapter 2 might be adopted, to give more satisfactory results in reconstruction parameter selection. The task of determining the human visual system MTF for a particular imaging and display system would necessarily become more problematic in this case.

Another source, [10], has also suggested calculating the geometric moments the band-limited power spectrum of an as an image quality measure:

$$IQM = \int_{\theta=0}^{2\pi} \int_{\rho=0}^{\rho_{upper}} \rho^n F(\rho, \theta) d\rho \quad (5.1)$$

or in discrete form

$$IQM = \sum_{\theta} \sum_{\rho=0}^{\rho_{upper}} \rho^n F(\rho, \theta) \quad (5.2)$$

where n is 2,3, or 4. This could also prove to be a valid metric, judging from Figure 2.3 in Chapter 2, since the "mass distributions" of a good image spectrum and a bad image spectrum are distinctly different. Note that if this turned out to be a valid IQM, it would not have the complication of requiring the user to determine the actual human visual system MTF. This IQM formulation was not tested in this thesis.

Another possible avenues of research could involve modifying the Sobel-Variance IQM by using other common edge enhancement filters such as the Roberts or Prewitt operators.

5.3 Conclusion

On all images tested, the Spectral and Sobel-Variance Image Quality Metrics give indications of being successful Image Quality Metrics for both raw and reconstructed images. Of course, the hypothesis that the Spectral and Sobel-Variance IQMs are valid measures of image quality can never be absolutely proven *per se*, but this thesis has lent weight to the hypothesis by showing that it has not been *disproven* for raw and reconstructed imagery for an interesting variety of satellite shapes. Therefore, the objectives of this research have been satisfied.

Appendix A. IQM Results for RORSAT and EORSAT Raw Imagery

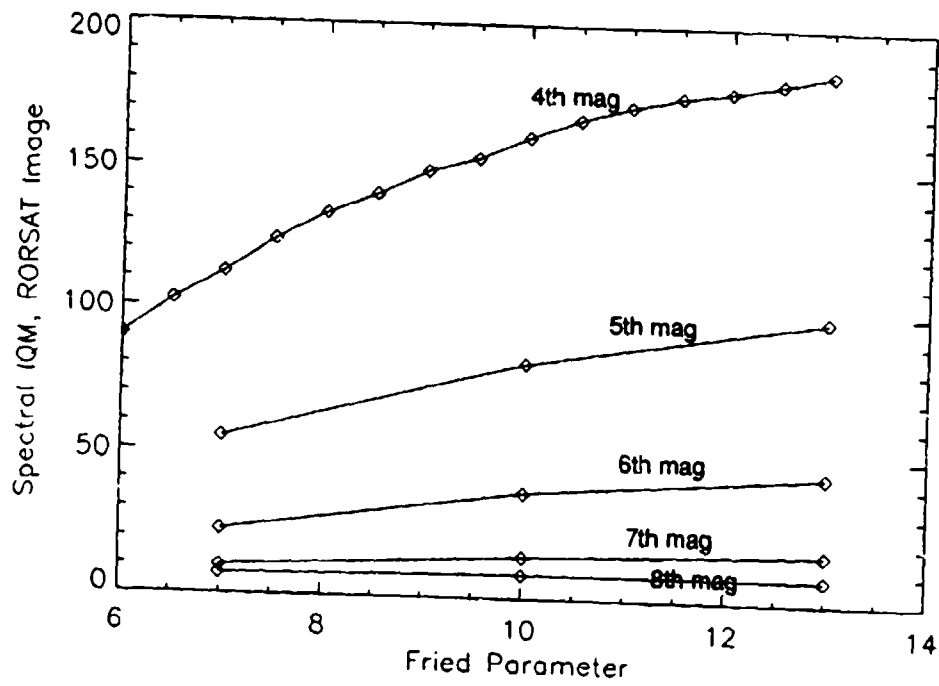


Figure A.1 Spectral IQM vs Fried Parameter, RORSAT Image

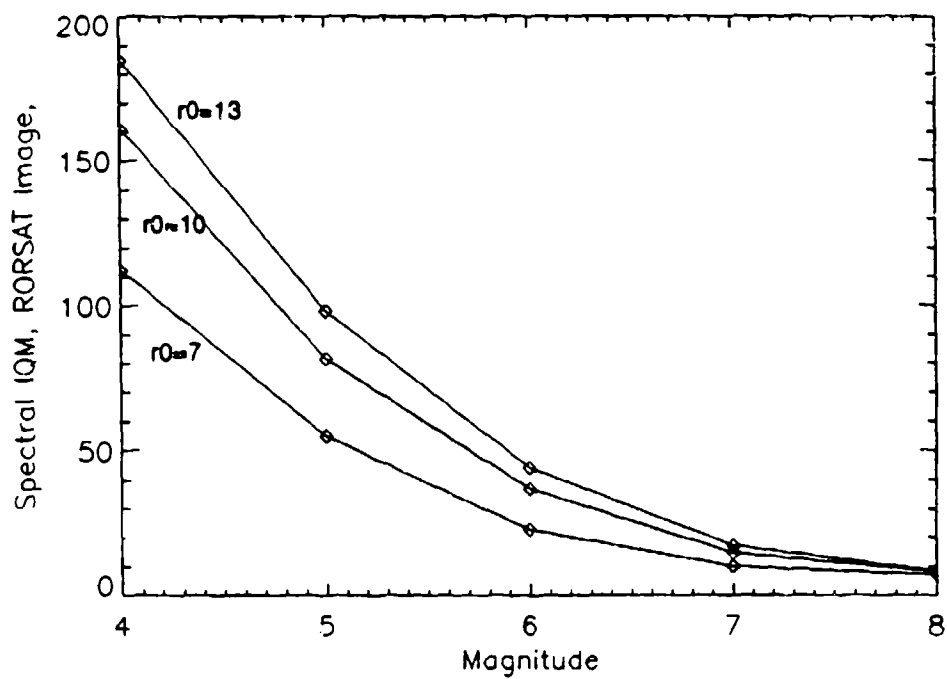


Figure A.2 Spectral IQM vs Target Magnitude, RORSAT Image

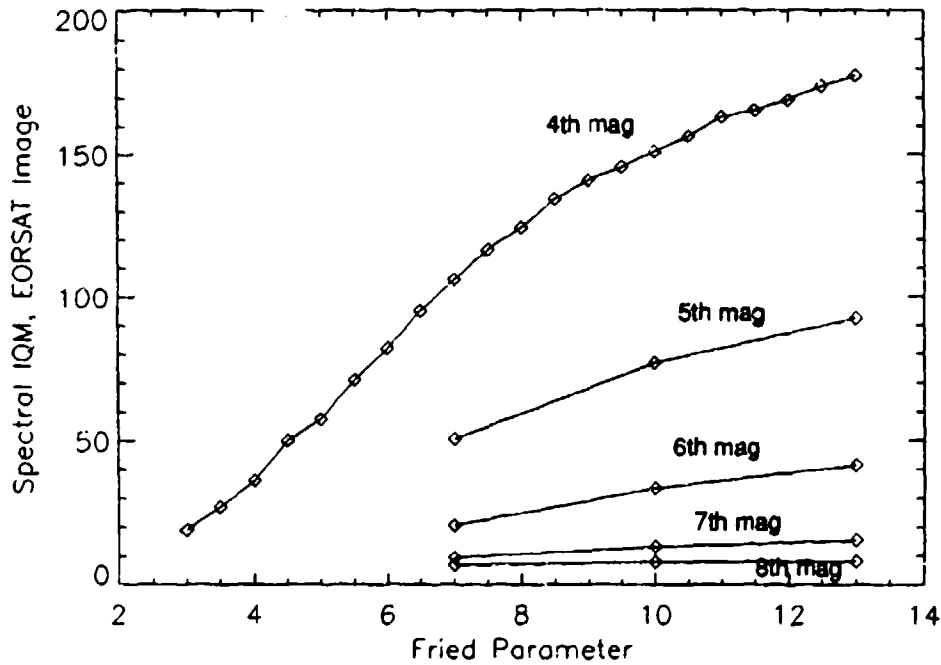


Figure A.3 Spectral IQM vs Fried Parameter, EORSAT Satellite Image

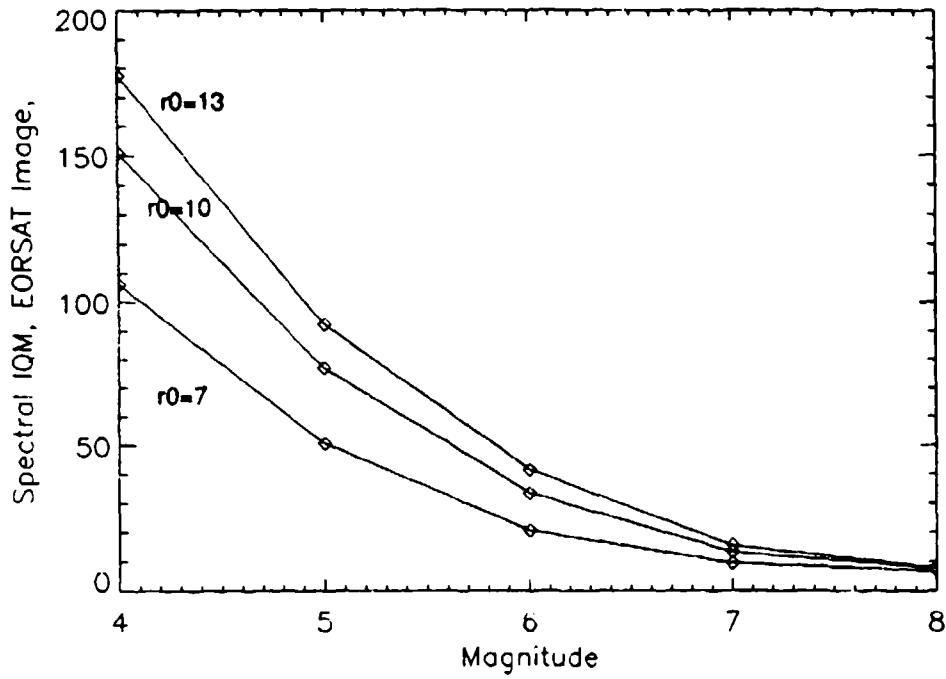


Figure A.4 Spectral IQM vs Target Magnitude, EORSAT Image

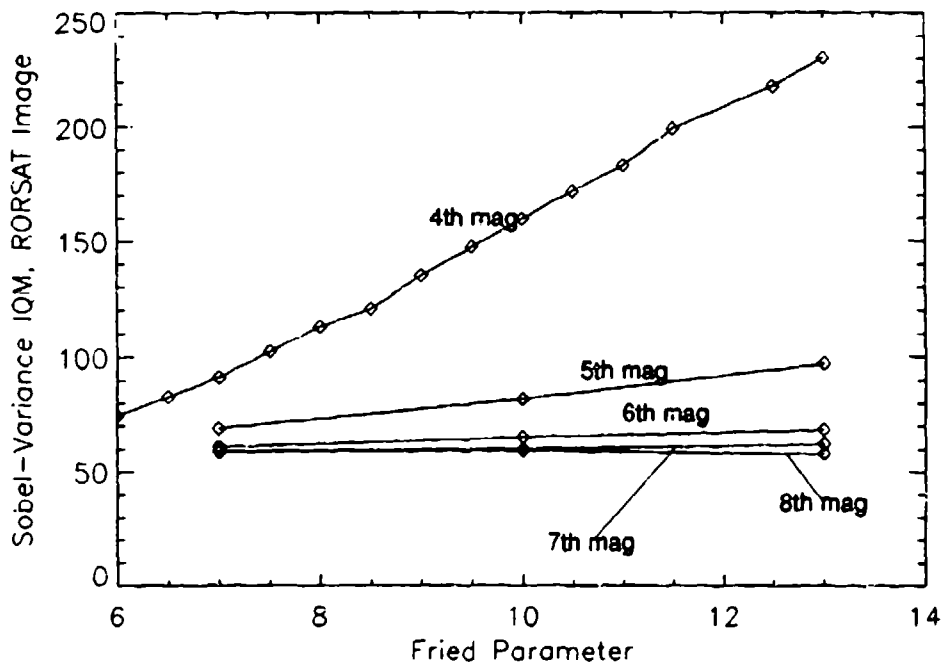


Figure A.5 Sobel-Variance IQM vs Fried Parameter, RORSAT Image

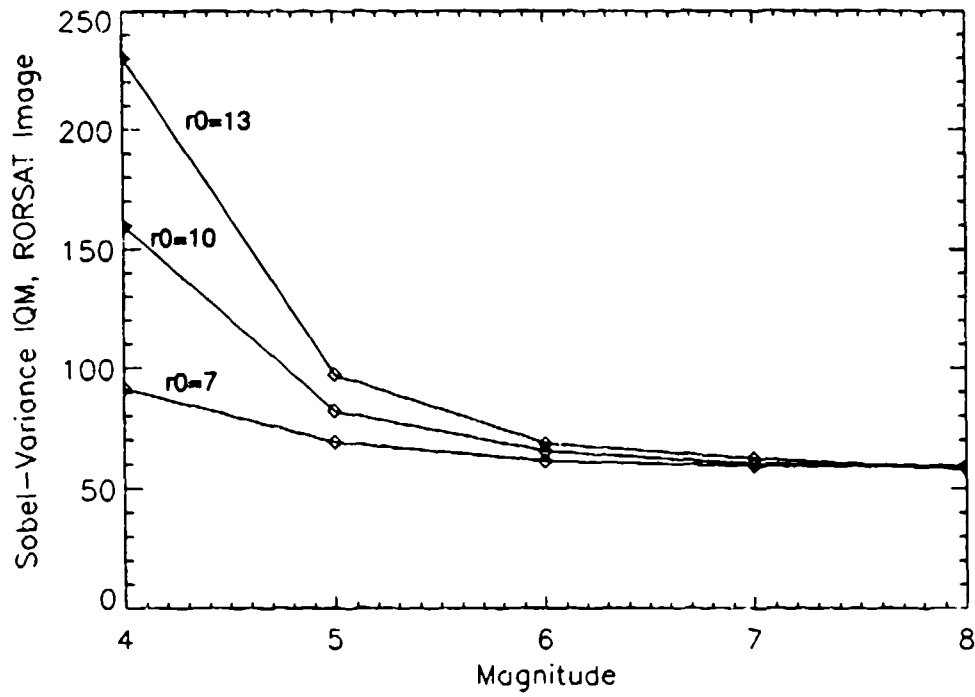


Figure A.6 Sobel-Variance IQM vs Target Magnitude, RORSAT Image

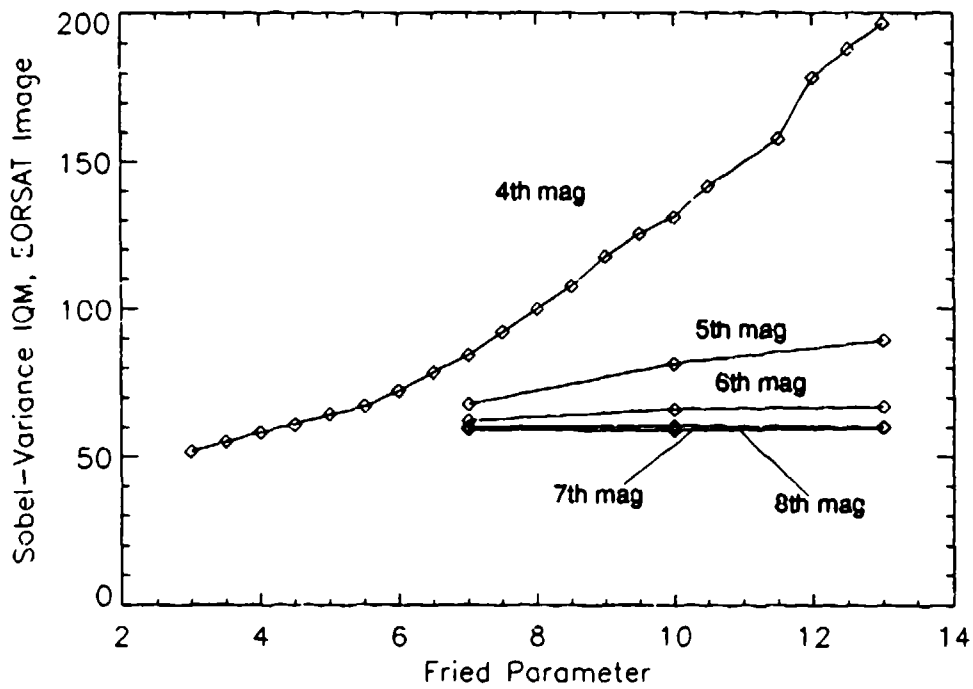


Figure A.7 Sobel-Variance IQM vs Fried Parameter, EORSAT Image

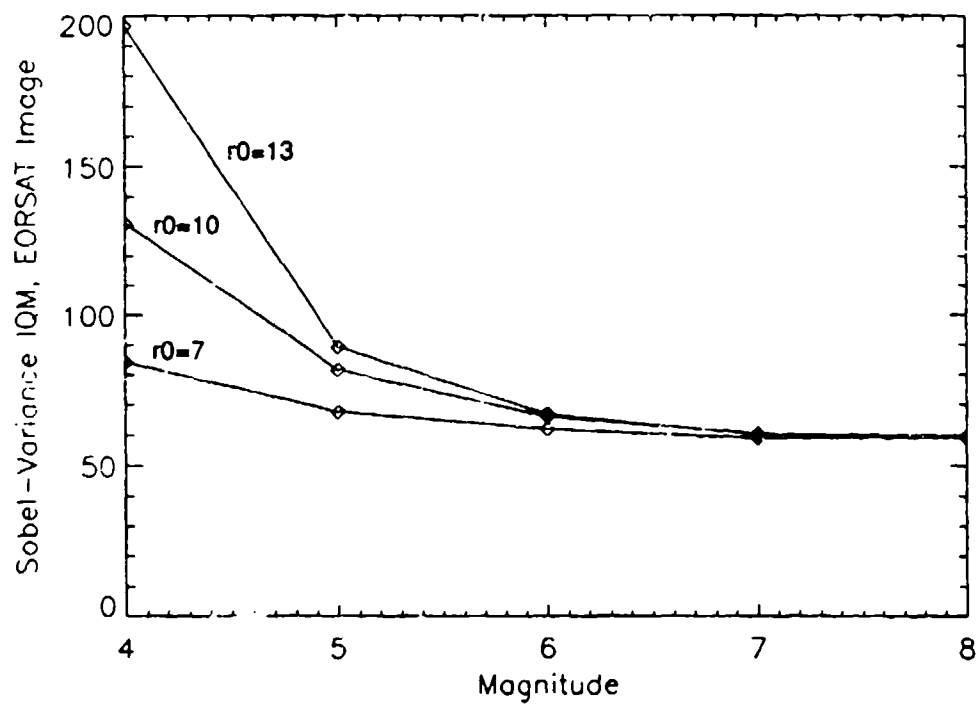


Figure A.8 Sobel-Variance IQM vs Target Magnitude, EORSAT Image

Bibliography

1. Beckers, Jacques M. "Adaptive Optics For Astronomy: Principles, Performance, and Applications," *Annual Reviews of Astronomy and Astrophysics*, 31:13 - 62 (1993).
2. Buffington, Andrew and R. A. Muller. "Real-time Correction of Atmospherically Degraded Telescope Images Through Image Sharpening," *Journal of the Optical Society of America*, 64:1200 - 1210 (September 1974).
3. Gaskill, Jack D. *Linear Systems, Fourier Transforms, and Optics*. New York: John Wiley & Sons, 1978.
4. Gonzalez, Rafael C. and Richard E. Woods. *Digital Image Processing*. New York: Addison-Wesley Publishing Company, 1992.
5. Goodman, Joseph W. *Statistical Optics*. New York: John Wiley & Sons, 1985.
6. Jain, Anil K. *Fundamentals of Digital Image Processing*. Englewood Cliffs, New Jersey: Prentice Hall, 1989.
7. Kegelmeyer, W.P. and Fred Hansen. "Automated Visual Quality Evaluation of CVD Film," *SPIE, Applications of Artificial Intelligence X: Machine Vision and Robotics*, 1708:88 - 98 (1992).
8. Linfoot, E. H. *Fourier Methods in Optical Image Evaluation*. New York: Focal Press.
9. Narayan, Ramesh and Rajaram Nityananda. "Maximum Entropy Image Restoration in Astronomy," *Annual Reviews of Astronomy and Astrophysics*, 24:127 - 170 (1986).
10. Nill, Norman B. "Scene Power Spectra: The Moment as an Image Quality Merit Factor," *Applied Optics*, 15:2846 - 2854 (November 1976).
11. Nill, Norman B. "A Visual Model Weighted Cosine Transform for Image Compression and Quality Assessment," *IEEE Transactions on Communications*, COMM - 33:551 - 557 (June 1985).
12. Nill, Norman B. and Brian H. Luzzas. "Objective Image Quality Measure Derived from Digital Image Power Spectra," *Optical Engineering*, 31:813 - 825 (April 1992).
13. Operations, AVCO Research Laboratory Maui. *AMOS User's Manual*. Technical Report AERILM 1176, Rev. 9, Griffiss AFB, NY 13441: Rome Air Development Center/OCSP, September 1990.
14. Research Systems, Inc., 777 29th St., Ste. 302, Boulder, CO 80303. *IDL Reference Guide* (Version 3.0 Edition), January 1993.
15. Research Systems, Inc., 777 29th St., Ste. 302, Boulder, CO 80303. *IDL User's Guide* (Version 3.0 Edition), January 1993.

16. Roggemann, M.C. "Optical performance of fully and partially compensated adaptive optics systems using least-squares and minimum variance phase reconstructors," *Computers and Electrical Engineering*, 18:451 - 466 (1992).
17. Roggemann, M.C. and J A. Meinhardt. "Image Reconstruction by Means of Wave-Front Sensor Measurements in Closed-Loop Adaptive-Optics Systems," *Journal of the Optical Society of America, A*, 10:1996 - 2007 (1993).
18. Roggemann, M.C., et al. "Linear reconstruction of compensated images: theory and experimental results," *Applied Optics*, 31:7429 - 7441 (10 December 1992).
19. Saghri, John A., et al. "Image Quality Measure Based on Human Visual System Model," *Optical Engineering*, 28:813 - 818 (July 1989).
20. Sklar, Bernard. *Digital Communications, Fundamentals and Applications*. Englewood Cliffs, New Jersey: Prentice Hall, 1988.
21. Stoudt, C. *Statistical Implications of Frame Selection Rules on Image Reconstruction*. MS thesis, Air Force Institute of Technology (AU), Wright-Patterson AFB, OH, December 1993.
22. Suzuki, A., 1993. Air Force Institute of Technology, Thesis Topic Proposal, Problem Statement, Internal Document.

Vita

Captain David J. Lee was born on May 19, 1965, in Watford City, North Dakota. He was raised on a farm outside of this small town in western North Dakota. After graduating from Watford City High School (with Honors) in 1983, he attended North Dakota State University in Fargo North Dakota on Air Force ROTC and National Merit scholarships. He graduated with honor as a Bachelor of Science in Electrical and Electronics Engineering in 1987. Entering Air Force active duty as a Second Lieutenant in 1988, David attended Undergraduate Space Training at Lowry AFB in Denver, Colorado for 5 months and then was assigned to the 1000th Satellite Operations Group as a Satellite Operations Officer. This unit operates the Defense Meteorological Satellite Program (DMSP). David was assigned to the Satellite Engineering Office, where he worked as a satellite and ground system software analyst and troubleshooter, and eventually became the chief of his section, supervising 2 officers and 2 enlisted men. During his tenure there he supervised his unit's preparation for the post-launch deployment of 2 DMSP satellites. In 1992, he was accepted into the Air Force Institute of Technology's Graduate Space Operations master's degree program, from which he graduated in December of 1993.

Permanent address: 1014 Middy Drive, WPAFB, OH 45433

REPORT DOCUMENTATION PAGE

Form Approved
OMB No 0704-0188

Public reporting burden for this collection of information is estimated to average 1 hour per response, including the time for reviewing instructions, searching existing data sources, gathering and maintaining the data needed, and completing and reviewing the collection of information. Send comments regarding this burden estimate or any other aspect of this collection of information, including suggestions for reducing this burden, to Washington Headquarters Services, Directorate for Information Operations and Reports, 1215 Jefferson Avenue, Suite 1204, Washington, DC 20543-4102, and to the Office of Management and Budget, Paperwork Reduction Project (0704-0188), Washington, DC 20503.

1. AGENCY USE ONLY (Leave blank)	2. REPORT DATE December 1993	3. REPORT TYPE AND DATES COVERED Master's Thesis
4. TITLE AND SUBTITLE OBJECTIVE IMAGE QUALITY METRICS: APPLICATIONS TO PARTIALLY COMPENSATED IMAGES OF SPACE OBJECTS		5. FUNDING NUMBERS
6. AUTHOR(S) David J. Lee, Captain, USAF		8. PERFORMING ORGANIZATION REPORT NUMBER AFIT/GSO/ENP/93D-03
7. PERFORMING ORGANIZATION NAME(S) AND ADDRESS(ES) Air Force Institute of Technology, WPAFB OH 45433-6583		10. SPONSORING MONITORING AGENCY REPORT NUMBER
9. SPONSORING MONITORING AGENCY NAME(S) AND ADDRESS(ES)		11. SUPPLEMENTARY NOTES
12a. DISTRIBUTION AVAILABILITY STATEMENT Approved for public release; distribution unlimited		12b. DISTRIBUTION CODE

13. ABSTRACT
 This thesis dealt with the automatic evaluation of the quality of a digital image by computer. Specifically, images of space objects as captured by a ground based adaptive optics telescope. Methods of measuring image quality included measuring the spectral content of an image within the bandpass of the human visual system and measuring the sharpness (variance) of edge-enhanced images. Selection of optimum reconstruction parameters was also addressed.

14. SUBJECT TERMS Image Processing, Image Assessment, Adaptive Optics, Space Surveillance, Space Object Identification	15. NUMBER OF PAGES 86
16. SECURITY CLASSIFICATION OF THIS PAGE Unclassified	15. PRICE CODE
17. SECURITY CLASSIFICATION OF ABSTRACT Unclassified	16. LIMITATION OF ABSTRACT UL